The Company of
Biologists

RESEARCH ARTICLE

A facilitated diffusion mechanism establishes the *Drosophila* Dorsal gradient

Sophia N. Carrell[‡], Michael D. O'Connell[‡], Thomas Jacobsen, Amy E. Pomeroy[*], Stephanie M. Hayes and Gregory T. Reeves[§]

ABSTRACT

The transcription factor NF-κB plays an important role in the immune system, apoptosis and inflammation. Dorsal, a *Drosophila* homolog of NF-κB, patterns the dorsal-ventral axis in the blastoderm embryo. During this stage, Dorsal is sequestered outside the nucleus by the IκB homolog Cactus. Toll signaling on the ventral side breaks the Dorsal/ Cactus complex, allowing Dorsal to enter the nucleus to regulate target genes. Fluorescent data show that Dorsal accumulates on the ventral side of the syncytial blastoderm. Here, we use modeling and experimental studies to show that this accumulation is caused by facilitated diffusion, or shuttling, of the Dorsal/Cactus complex. We also show that active Toll receptors are limiting in wild-type embryos, which is a key factor in explaining global Dorsal gradient formation. Our results suggest that shuttling is necessary for viability of embryos from mothers with compromised *dorsal* levels. Therefore, Cactus not only has the primary role of regulating Dorsal nuclear import, but also has a secondary role in shuttling. Given that this mechanism has been found in other, independent, systems, we suggest that it might be more prevalent than previously thought.

KEY WORDS: Morphogen, Tissue patterning, Mathematical modeling, Dorsal, Cactus, Shuttling

INTRODUCTION

In a developing organism, tissues are patterned by long-range signaling enacted through morphogen concentration gradients, which carry the positional information necessary to control gene expression in a spatially dependent manner. The mechanisms by which morphogen concentration gradients form has been an area of intense study (Wartlick et al., 2009; Smith, 2009; Matsuda et al., 2016; Müller et al., 2013; Christian, 2012; Guerrero and Kornberg, 2014). For example, in the *Drosophila* wing disc, there are conflicting theories for Dpp gradient formation, including receptor-mediated transcytosis, (restricted) diffusion and cytonemes (Entchev et al., 2000; Lander et al., 2002; Schwank et al., 2011; Matsuda et al., 2016; Belenkaya et al., 2004; Roy et al., 2014). In the *Drosophila* syncytial blastoderm, the anterior-posterior (AP) Bicoid gradient, perhaps the most well-studied morphogen gradient system, has long been thought to develop through a mechanism of diffusion from a spatially localized source (Driever and Nüsslein-Volhard, 1988; Houchmandzadeh et al.,

Department of Chemical and Biomolecular Engineering, North Carolina State University, Raleigh, NC 27605, USA.
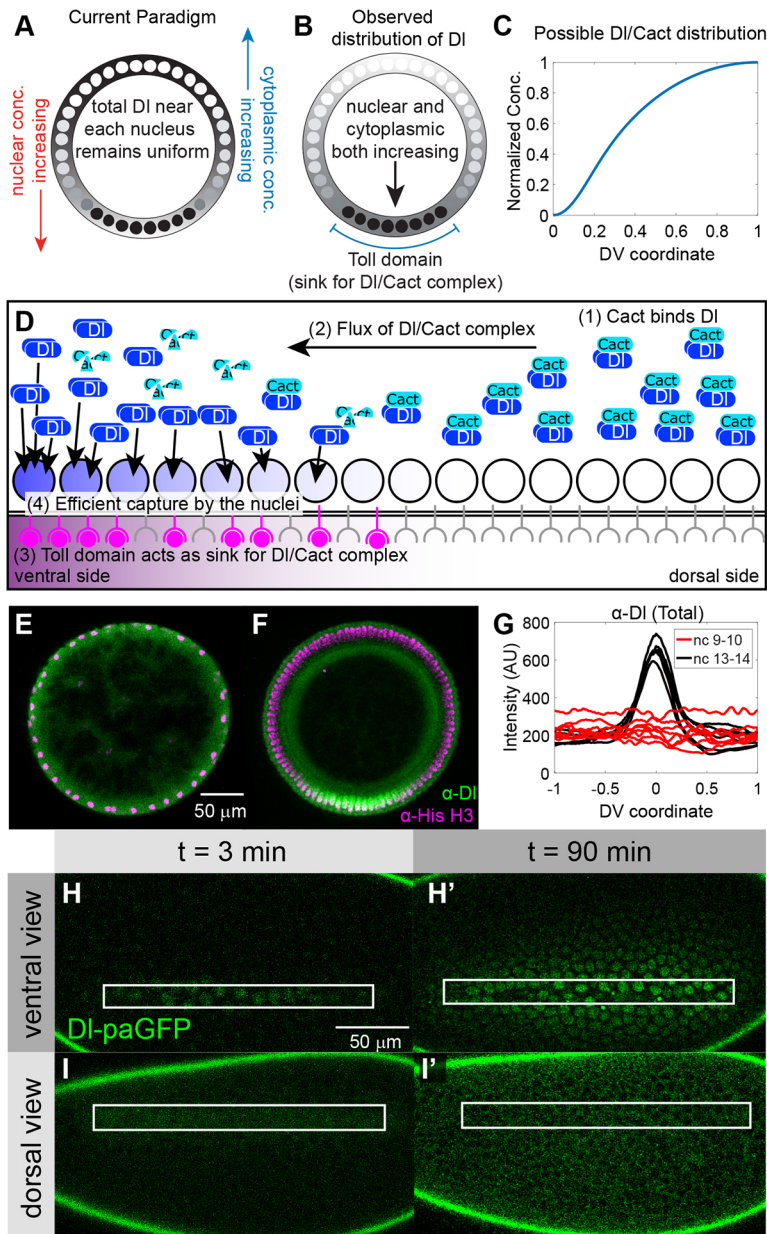*Present address: Curriculum in Bioinformatics and Computational Biology, University of North Carolina, Chapel Hill, NC 27599, USA.
[‡]These authors contributed equally to this work

[§]Author for correspondence (gtreeves@ncsu.edu)

G.T.R., 0000-0003-0836-7766

2002; Gregor et al., 2005, 2007; Little et al., 2011). More recently, it has been proposed that the Bicoid gradient develops largely from a *bicoid* mRNA gradient, which itself developed through active transport (Spirov et al., 2009; Fahmy et al., 2014; Ali-Murthy and Kornberg, 2016).

During the same stages in which Bicoid patterns the AP axis, the maternally provided transcription factor Dorsal (Dl), which is natively found as a homodimer (Govind et al., 1992; Isoda et al., 1992; Whalen and Steward, 1993; Drier et al., 2000), also acts as a morphogen to regulate the spatial patterns of >50 genes along the dorsal-ventral (DV) axis (Reeves and Stathopoulos, 2009; Moussian and Roth, 2005; Chopra and Levine, 2009). Both *dl* mRNA and Dl protein are maternally deposited into the embryo, and Dl protein is initially uniformly distributed around the DV axis (Steward et al., 1988; Roth et al., 1989). During nuclear cycle (nc)10, when the nuclei migrate to the periphery of the syncytial blastoderm, a nuclear concentration gradient of Dl develops, with high concentrations in the ventral nuclei, graded levels in ventral-lateral (VL) nuclei, and basal levels in the nuclei on the dorsal half of the embryo (Roth et al., 1989; Liberman et al., 2009; Reeves et al., 2012). In the ventral 20% of the embryo, the highest levels of Dl are achieved, and, as a result, high threshold genes, such as *twist* (*twi*) and *snail* (*sna*) are activated, which are required to specify the future mesoderm (Stathopoulos and Levine, 2002; Reeves and Stathopoulos, 2009; Chopra and Levine, 2009). Intermediate threshold genes, such as *vnd* and *rhomboid*, are expressed in VL domains, and low threshold genes, such as *sog* and *dpp*, have boundaries at ∼50% of the way around the DV axis.

The mechanisms by which the Dl nuclear concentration gradient develops are well known, partly because Dl is one of three *Drosophila* homologs of NF-κB. At the single nucleus/cell level, Dl is sequestered to the cytoplasm in an inactive complex with the IκB homolog Cactus (Cact). On the ventral side of the embryo, signaling through the Toll receptor results in the degradation of Cact, freeing Dl to enter the nucleus, where it regulates transcription (Belvin et al., 1995; Bergmann et al., 1996; Reach et al., 1996; Whalen and Steward, 1993). *cact* mutant embryos still develop a shallow Dl gradient (Bergmann et al., 1996; Roth et al., 1991; Cardoso et al., 2017), probably due to a weak bias in Dl nuclear import from Toll signaling (Drier et al., 1999, 2000). The weakly polarized DV axis in the absence of Cact activity can also be seen in the Dl target gene expression domains, which are altered, but retain some DV polarity (Roth et al., 1991; Cardoso et al., 2017).

Cytoplasmic sequestration of Dl by Cact, combined with a ventral-to-dorsal gradient of Toll signaling, is sufficient to develop a gradient of nuclear Dl concentration, and is evidently the primary driving force for the formation of spatial asymmetry in Dl nuclear concentration. However, taken alone, this mechanism would result in a local depletion of Dl from the cytoplasm surrounding the ventral nuclei to create a counter-gradient in cytoplasmic Dl (Roth et al., 1989) (Fig. 1A). This paradigm is implicitly accepted, and has been

DEVELOPMENT

Fig. 1. Dorsal accumulates on the ventral side of the embryo.
(A) Current paradigm of Dl distribution states that total Dl levels are uniform throughout the embryo. (B) Fluorescent images suggest that total Dl accumulates on the ventral side. 'Toll domain' indicates the location at which Toll receptors are being activated.
(C) Possible protein gradient of cytoplasmic Dl/Cact complex. The Dl/Cact complex is expected to have an inverse gradient owing to the ventral Toll domain. (D) Schematic of the shuttling mechanism. Toll-mediated degradation of Cact on the ventral side results in a concentration gradient of Dl/Cact complex, which in turn results in a net flux of Dl/Cact to the ventral side. Free Dl does not diffuse back to the dorsal side because it is efficiently captured by the nuclei. Numbers indicate the four biophysical processes necessary for shuttling. (E) Cross section of an nc 10 wild-type embryo, stained for Dl and nuclei. Dl is equally distributed throughout the embryo. (F) Total Dl has accumulated at the ventral midline by late nc 14. (G) Quantification of total α-Dl fluorescence in nc 9-10 (red) and nc 13-14 (black) embryos. (H-I') Photoactivation of embryos from mothers carrying one copy of wild-type (wt) Dl and one copy of Dl-paGFP indicates that Dl diffuses throughout the embryo. The activation area is within the white boxes; anterior to the left. Panels show activation near the ventral midline ~3 min (H) and 90 min (H') after first activation, and activation near the dorsal midline ~3 min (I) and 90 min (I') after first activation. See also Movies 1 and 2, Fig. S1.

depicted many times in the literature (e.g. in Haskel-Ittah et al., 2012; Rushlow and Shvartsman, 2012). However, this paradigm is in contrast to recent observations that nuclear+cytoplasmic levels of Dl fluorescence accumulate on the ventral side of the embryo over time (Reeves et al., 2012) (Fig. 1B). It is important to note that fluorescence measurements of Dl likely do not distinguish between free Dl and bound Dl (Dl/Cact complex). The mechanism by which this ventral accumulation of total Dl (defined henceforth as the sum of local nuclear+cytoplasmic levels of bound+free Dl) takes place remains unknown, as does the question of whether accumulation is necessary for proper gene expression patterning and the fitness of the embryo.

One possible mechanism is that the hypothesized counter-gradient in cytoplasmic Dl, mentioned above, might drive free Dl to diffuse to the ventral side. However, this is unlikely to be the case, as the predominant Dl-containing species on the dorsal side of the embryo should be Dl/Cact complex, not free Dl. Therefore, we propose that the ventral accumulation of total Dl occurs by a facilitated diffusion, or 'shuttling' mechanism via Dl/Cact complex

(Shilo et al., 2013). According to this mechanism, a carrier molecule (Cact) helps to shuttle the morphogen up its concentration gradient so that it may accumulate in one location. In the Dl/Cact system, the shuttling hypothesis states that a dorsal-to-ventral concentration gradient of cytoplasmic Dl/Cact complex develops as the result of Toll-mediated degradation of Cact, which in turn results in ventrally directed flux of Dl (Fig. 1C).

The shuttling mechanism has been previously described and is responsible for gradient formation in the Dpp/BMP signaling pathway (Ben-Zvi et al., 2008; Eldar et al., 2002; Holley et al., 1996; Marqués et al., 1997; Mizutani et al., 2005; Shimmi et al., 2005; Wang and Ferguson, 2005; Ashe and Levine, 1999; Dorfman and Shilo, 2001; Umulis et al., 2006). It has also been suggested for the formation of the Spätzle gradient upstream of Toll signaling (Haskel-Ittah et al., 2012). It should be noted that the Dl/Cact system has each of the four features required for shuttling to occur in the embryo (Fig. 1D) (Shilo et al., 2013): (1) the primary molecule (Dl) binds to a 'carrier' molecule (Cact) that protects it from capture/

degradation; (2) the primary/carrier complex is diffusible on a global scale (shown in this study); (3) the complex is broken in a spatially dependent manner (through Toll signaling on the ventral side of the embryo); and (4) when free of the carrier, the primary molecule is captured (in this case, by the nuclei) or degraded.

The main analysis in this paper was performed using a combination of computational model predictions and experimental validation to support the shuttling hypothesis. To this end, we first demonstrated that Dl diffuses globally throughout the embryo, so that each of the four criteria above are met for the Dl/Cact system. Next, we used a simplified version of previously published computational models (O'Connell and Reeves, 2015; Kanodia et al., 2009; Ambrosi et al., 2014) to predict the outcome of experiments in which shuttling is compromised by lowering Dl diffusion: depending on the severity of the perturbation, the Dl gradient widened, became flat on top, or split into two peaks (i.e. there was no longer a single peak at the ventral midline). Through careful analysis of BAC-recombineered, GFP-tagged Dl constructs, which slow the mobility of Dl, we validated the predicted outcomes of the shuttling hypothesis. The same three phenotypes are also seen in embryos from *dl* heterozygous mothers, in embryos with a widened Toll domain, and in embryos with an ectopically expressed, AP Dl gradient (Liberman et al., 2009; Roth and Schüpbach, 1994; Huang et al., 1997). To account for these phenotypes, we extended our simplified model to take into account the possibility that active Toll receptors are limiting in the VL regions of the Toll domain. The extended Toll saturation model successfully explained the phenotypes in those three sets of embryos. We experimentally validated the Toll saturation assumption by showing that the single, curved Dl gradient peak is restored in *dl* heterozygotes by lowering the maternal *Toll* dosage, as well as in embryos with a wide Toll domain, by increasing the dosage of Dl.

Our data show that shuttling does occur, and that it is necessary when maternal *dl* levels are compromised. Although *dl* heterozygous mothers in an otherwise wild-type background are not sterile, we showed that embryos from mothers carrying a single copy of *dl-GFP* and zero endogenous copies of *dl* are nonviable, owing to severe shuttling-based defects in the Dl gradient and the consequent failure to express *sna* in a sufficient number of ventral cells. The data are less clear as to whether shuttling is necessary for embryonic fitness when maternal *dl* levels are not compromised (Roth et al., 1991; Cardoso et al., 2017). Even so, we argue that the data, on balance, favor the necessity of the shuttling mechanism in wild-type embryos. We conclude that, in addition to its primary role of regulating Dl entry into the nucleus, Cact performs a secondary, but important, role in Dl gradient formation: shuttling Dl to the ventral side to form the mature gradient.

RESULTS

Dl accumulation on the ventral side of the embryo results from movement of Dl

Initially, Dl is uniformly distributed along the DV axis of the developing embryo (Roth et al., 1989) (Fig. 1E,G); during nc 11-14, it accumulates on the ventral side (Fig. 1F,G). This observation is consistent with previously published fluorescent images of anti-Dl immunostaining in fixed embryos and in images of Dl-GFP fluorescence in live embryos (Kanodia et al., 2009; Reeves and Stathopoulos, 2009; Liberman et al., 2009; Reeves et al., 2012). In particular, live imaging of a Dl-Venus construct in optical cross sections showed that, even during mitosis, when the nuclear concentration gradient is abolished, there is a bias of total Dl on the ventral side (Reeves et al., 2012). To measure this bias, we imaged and quantified cross sections of fixed younger (nc 9-10) embryos (Fig. 1E) and

compared their total Dl distribution to similar quantifications of older (nc 13-14) embryos (Fig. 1F). We found that, in younger embryos, total Dl was distributed evenly throughout the embryo, while older embryos displayed a total Dl gradient with a strong ventral peak, similar to quantifications of the Dl nuclear concentration gradient (Fig. 1G).

The mechanism for this overall polarization of total Dl in the embryo could stem from net flux of Dl to the ventral side of the embryo. Previous work showed that, on short time scales (seconds), the free diffusion of Dl-GFP is rapid enough that nucleocytoplasmic compartments (the regions surrounding a single nucleus) appear well mixed, while there are barriers to movement between neighboring nucleocytoplasmic compartments (Delotto et al., 2007). On the other hand, on longer time scales (minutes), exchange between nucleocytoplasmic compartments is possible, which we consider behaves like diffusion on coarse length scales. To confirm the global movement of Dl throughout the embryo (hereafter referred to simply as diffusion), we used a photoactivatable GFP (paGFP) tag (Patterson and Lippincott-Schwartz, 2002), and noticed that Dl appears in regions of the embryo >7-10 nuclei away from the site of paGFP activation over a time span of 90 min (Fig. 1H,I; Fig. S1), during which the activation region was under near-constant photoactivation (see Materials and Methods). The distance over which activated Dl can spread appears to depend on the region of the embryo. When activated near the ventral midline, Dl-paGFP moves from its location of activation and fills adjacent nuclei, extending ∼6-7 nuclei away (Fig. 1H,H′; Movie 1). When activated on the dorsal side of the embryo, Dl-paGFP can eventually be seen in all nuclei in view, and shows a typical pattern of exclusion from nuclei in more dorsal regions and moderate uptake into the nuclei in more lateral regions (Fig. 1I,I′; Movie 2). The difference in mobility is likely to be caused by nuclear capture of free Dl on the ventral side. In any case, our observation of global movement of Dl within the embryo provides the final, previously unconfirmed, physical process necessary for shuttling to occur.

Model analysis and experimental prediction

To determine whether the four biophysical processes outlined in the Introduction are sufficient to drive the accumulation of Dl on the ventral side of the embryo, we analyzed a simplified model of Dl/Cact/Toll interactions in the early embryo (Fig. 2A). Our model included partial differential equations for four species: nuclear Dl, cytoplasmic Dl, cytoplasmic Cact, and cytoplasmic Dl/Cact complex (see Materials and Methods). These equations describe the processes of Dl/Cact binding (k_{bind}); the production (V_{cact}; not shown in Fig. 2A) and degradation of Cact (k_{deg}); the nuclear import/export of Dl (k_{in}, k_{out}); the Toll-mediated dissociation of the Dl/Cact complex (k_{diss}); and the intercompartmental movement of cytoplasmic species (D; Fig. 2A). The catalytic activity of Toll signaling was modeled phenomenologically by allowing k_{diss} to be a function of x: $k_{diss}(x)=k_{diss,0}\exp(-0.5x^2/\phi^2)$, where β models the strength of Toll signaling and ϕ is a parameter that controls the spatial extent of Toll signaling.

We quantitatively defined shuttling as the scenario in which there is a net flux of Dl-containing species to the ventral 33% of the embryo (see Materials and Methods). We simulated 10^5 randomly chosen data sets from among reasonable allowed variations in parameter values (see Supplementary Materials and Methods) and examined under what conditions shuttling would occur. We found that the diffusivity of the Dl/Cact complex (D_{DC}) must be greater than the effective diffusivity of free Dl for shuttling to occur. In our simplified model, nuclear and cytoplasmic Dl are assumed to be in equilibrium, which makes the effective diffusivity of Dl $D_{Dl}^{eff}=D_{Dl}/(1+K_{eq})$, where $K_{eq}=k_{in}/k_{out}$ (see Supplementary Materials and
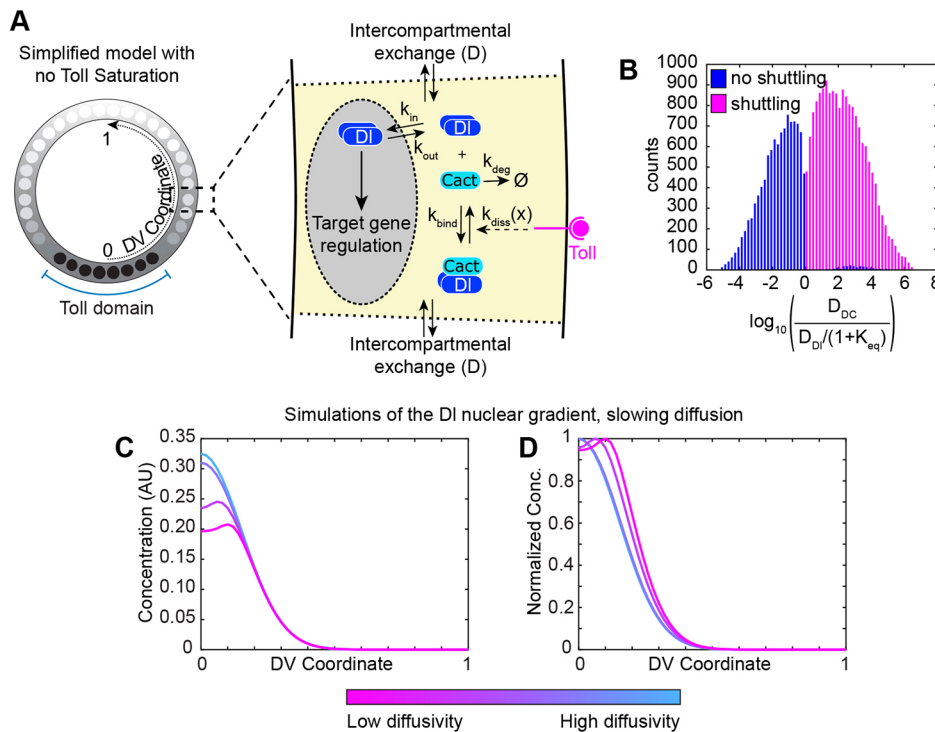
Fig. 2. Model for predicting a shuttling mechanism and mutant phenotypes. (A) Simplified model of Dl gradient dynamics in which Toll is not saturable. (B) Parameter sets for which shuttling occurs are nearly perfectly identified by the inequality $D_{DC}/[D_{Dl}/(1+K_{eq})]>1$, where $D_{Dl}/(1+K_{eq})$ represents the effective diffusivity of free Dl under equilibrium conditions. (C) Slowing diffusion to reduce rate of shuttling results in a hallmark progression of phenotypes. The Dl gradient widens (width parameter σ increases), flattens at the peak, or obtains a split peak (i.e. the peak is no longer at the ventral midline). (D) Dl gradients found in C, normalized. The normalization reveals the widening of the gradients. Colorbar indicates strength of perturbation. See also Fig. S2.

Methods for more details). In other words, shuttling occurs when $D_{DC}/D_{Dl}^{eff}>1$ (Fig. 2B). This is relatively unsurprising, as the Dl/Cact complex must be able to diffuse toward the ventral midline more efficiently than free Dl can diffuse away. Furthermore, difference in diffusivities between the free activator and the inhibitory complex has previously been shown to be a hallmark of a shuttling system (Eldar et al., 2002). The equilibrium constant for nuclear import also plays an important role because nuclear capture of free, cytoplasmic Dl must be sufficiently strong to prevent Dl from diffusing back to the dorsal side of the embryo (Fig. 1D). See Supplementary Materials and Methods for more details.

Further analysis of our model showed that the mechanism of facilitated diffusion can be tested by slowing diffusion of the Dl/Cact complex. The model predicts that different instances in a hallmark series of phenotypes will be observed, depending on the severity of the perturbation. In order of increasing strength of perturbation: the Dl gradient widens, becomes flat on top, or splits into two peaks (Fig. 2C, D). These predictions and the shuttling phenomenon itself arise naturally out of biophysical processes known to occur in the embryo: global movement, binding of Dl and Cact, Toll-mediated destruction of the Dl/Cact complex on the ventral side, and nuclear capture of free Dl. Indeed, previous models of the Dl gradient, which included these processes, also exhibit shuttling, even when it was not considered in the models (Fig. S2, Supplementary Materials and Methods) (Kanodia et al., 2009; Ambrosi et al., 2014; O'Connell and Reeves, 2015). In particular, in previous work using a model of the Dl/Cact system, the authors found that increasing the diffusion rate caused the gradient to sharpen (Ambrosi et al., 2014), which is the same prediction detailed here (Fig. 2C,D). We analyzed the model presented in that study, and show that this result arose because shuttling was indeed occurring in that model, even though the authors did not intend it to be (Fig. S2).

Decreased diffusion of the Dl/Cact complex widens the Dl gradient

Our approach to slowing the diffusion of the Dl/Cact complex was to tag Dl with a bulky protein domain. Multiple versions of Dl tagged with

GFP variants have been made to study Dl gradient dynamics in living embryos (Delotto et al., 2007; Reeves et al., 2012); in two instances, GFP tags caused the Dl gradient to expand as predicted by the shuttling mechanism (Fig. 2C,D). Previous work has shown that tagging Dl with a monomeric Venus (Dl-mVenus) causes the Dl gradient to widen, while a GFP tag causes a much greater widening (Liberman et al., 2009; Reeves et al., 2012). We surmised that the difference between these scenarios is that Venus is an obligate monomer, whereas the GFP construct weakly dimerizes (Zacharias et al., 2002).

However, as these observations were comparing GFP to mVenus, we wished to investigate further by minimizing differences between the monomeric and dimeric GFP variants. Therefore, we constructed a transgenic fly line carrying a BAC-recombineered Dl tagged with monomeric GFP (Dl-mGFP; see Materials and Methods). The weak dimerization of GFP can be abolished by the A206K mutation, so that GFP[A206K] is an obligate monomer (Zacharias et al., 2002). Together with a wild-type fly line and a line carrying the Dl tagged with a GFP that weakly dimerizes (Dl-dGFP) (Reeves et al., 2012), this created an 'allelic series' of Dl constructs with progressively decreasing mobility. If the shuttling hypothesis is correct, we would expect that lowering the mobility would widen the gradient. First, we measured the gradient width in fixed wild-type embryos using an antibody against Dl and found the width parameter, σ, to be 0.147±0.002 (mean±s.e.m. here and elsewhere) (Fig. 3; Fig. S3A; see Supplementary Materials and Methods for a description of the width parameter) (Liberman et al., 2009; Reeves et al., 2012; Garcia et al., 2013).

Next, we investigated the Dl-mGFP embryos. These embryos are from dl, dl-mGFP/+ mothers (one copy of Dl-mGFP, one functional copy of endogenous Dl). Because Dl naturally self-associates (Govind et al., 1992; Isoda et al., 1992; Whalen and Steward, 1993; Drier et al., 2000), three species of Dl dimer would exist in these embryos: Dl:Dl, Dl:Dl-mGFP and Dl-mGFP:Dl-mGFP. Therefore, the effective, overall mobility of Dl in these embryos would be slightly lower than in wild type. As predicted by the shuttling hypothesis, these Dl-mGFP embryos have gradients slightly wider than wild type (σ=0.184±0.005; P=10⁻⁷; Fig. 3).
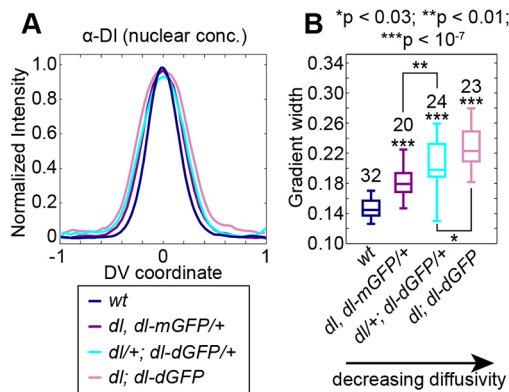
Fig. 3. Decreasing the diffusion of Dl/Cact increases the width of the Dl gradient. (A) Normalized average plots of the nuclear fluorescence of α-Dl in embryos with two copies of wt *dl* (wt, blue), one copy of wt *dl* and one copy of *dl-mGFP* (*dl, dl-mGFP/+*, purple), one copy of wt *dl* and one copy of *dl-dGFP* (*dl/+; dl-dGFP/+*, cyan), and zero copies of wt *dl* and two copies of *dl-dGFP* (*dl; dl-dGFP*, pink). (B) Box plot of gradient widths (σ) for the genotypes in A. Here and in Figs 4-6, boxes indicate interquartile range (IQR: from the 25th to the 75th percentile of the data); whiskers extend a maximum of 1.5 times the width of the IQR from the box; outliers (plus signs) are defined as points that lie outside the whiskers; numbers indicate sample size; asterisks without connecting lines indicate statistical difference from wild type. Colors match the scheme in A. See also Fig. S3.

Third, we investigated whether the Dl-dGFP embryos would have even wider gradients than the Dl-mGFP embryos. Therefore, we analyzed the gradient in embryos from mothers carrying one copy of *dl-dGFP* (Reeves et al., 2012) and heterozygous null for endogenous *dl* (genotype *dl/+; dl-dGFP/+*). In these embryos, heterodimers of endogenous Dl and Dl-dGFP might form weak interactions with similar heterodimers, which would result in larger groups of heterodimers with slower mobility. The situation is further exacerbated if the dimer happens to be a homodimer of Dl-dGFP, which should account for ~25% of the Dl dimer species. We found that the Dl gradient in these embryos widened significantly as compared to wild type (σ=0.207±0.007; $P=2\times10^{-9}$; Fig. 3).

Finally, we analyzed embryos completely lacking endogenous Dl and with two copies of Dl-dGFP (maternal genotype: *dl; dl-dGFP*). In these embryos, 100% of the Dl molecules are fused to dGFP, so that every Dl-containing dimer has the ability to weakly interact with two other Dl-dGFP dimers. As predicted by the shuttling hypothesis, the Dl gradients in these embryos were also widened compared to wild type (σ=0.228±0.008; $P=10^{-12}$; Fig. 3). Moreover, the 'allelic series' behaved as predicted: embryos with progressively less mobile Dl had progressively wider gradients.

To further test the predicted phenotype of slowing diffusion, we also examined embryos with Venus-tagged Dl (Reeves et al., 2012), β-galactosidase-tagged Dl (Govind et al., 1996) and β-galactosidase-tagged Cact (Fernandez et al., 2001). In each of these cases, the phenotype expected from the shuttling hypothesis was found (Supplementary Materials and Methods, Fig. S3B,C).

The length scale of a concentration gradient can be altered by changing the rate of capture (in this case, by the nuclei) in addition to diffusion. Therefore, we used a combination of photobleaching experiments, to measure the import and export rate of Dl-dGFP and Dl-mGFP, and modeling, to show that only perturbing diffusion, and not nuclear import/export, results in a shuttling-based phenotype (Fig. S3D-O, Movie 3, Supplementary Materials and Methods).

### Toll saturation allows decreasing Dl dosage to widen and flatten the Dl gradient

In embryos from mothers heterozygous null for Dl (hereafter referred to as *dl/+* embryos), the shape of the gradient becomes slightly wider and flatter, sometimes to the point of generating a double peak (Fig. 4A-D; note especially in Fig. 4B the local minimum at the ventral midline and local maxima elsewhere) (Liberman et al., 2009; Ambrosi et al., 2014). This phenotype bears striking resemblance to the model predictions for lowering diffusion (Fig. 2C,D); therefore, we investigated whether the shuttling mechanism could possibly explain the phenotype in *dl/+* embryos. However, model simulations showed that reducing the *dl* dosage could not significantly change the width or the shape of the Dl gradient, much less result in a double peak (Ambrosi et al., 2014) (Fig. S4A-D).

One mechanism that could explain this phenotype is saturation of active Toll receptors. If the domain of active Toll signaling is graded in space (Haskel-Ittah et al., 2012; Rahimi et al., 2016), active Toll receptors should be limiting at the domain edge. If active Toll saturation is sufficiently extensive in wild-type embryos, then the formation of a smooth peak is the result of sufficient numbers of Dl/Cact complexes bypassing the saturated Toll regime and arriving at the ventral midline (Fig. 4E). However, in *dl/+* embryos, less Dl implies fewer Dl/Cact complex molecules will arrive at the ventral midline (Fig. 4F), resulting in a wider, flatter and sometimes split peak of nuclear Dl. However, previous models did not account for this possibility because the rate of Toll-mediated Cact degradation was assumed to be proportional to the concentration of Dl/Cact, creating a potentially unlimited sink, even at the edges of the active Toll domain (O'Connell and Reeves, 2015; Kanodia et al., 2009; Ambrosi et al., 2014). Therefore, we extended our simplified mathematical model (Fig. 2A) to account for the possibility that active Toll receptors numbers are limiting (Fig. 4G; see Materials and Methods). In the remainder of this paper, we use this extended model. When active Toll receptors are saturable, simulated *dl/+* embryos have widened, flattened gradients (Fig. S4E,F).

To experimentally test whether active Toll receptors are limiting, we compared Dl gradients in wild-type embryos and *dl/+* embryos with those from *dl/+; Tl/+* mothers (hereafter *dl/+; Tl/+* embryos). In *dl/+; Tl/+* embryos, reducing the Toll dosage should partially 'rescue' the saturation of the active Toll receptor, and thus result in a smoother Dl gradient peak at the ventral midline. We found that the profile of total Dl in these embryos is, on average, more smoothly peaked (Fig. 4H; Fig. S4G-I). To determine whether the gradient peaks are different in *dl/+* versus double-heterozygote embryos, we calculated two measures of peak shape: location of peak (Fig. 4I,J) and intensity of the peak at the ventral midline (Fig. 4I,K). In both cases, the *dl/+* embryos were statistically different from the *dl/+; Tl/+* embryos, which validates our hypothesis that active Toll receptors are limiting.

Perturbing both mobility and dosage has a combined effect

Our model also predicts that simultaneously lowering both dosage and mobility would have a combined effect on the severity of the shuttling phenotype. To test this hypothesis experimentally, we investigated embryos from mothers that carry a single copy of *dl-dGFP* and no endogenous *dl* (*dl; dl-dGFP/+*). In our and previous studies, this genotype is observed to be female sterile; two copies of *dl-dGFP* are necessary to rescue the mutant (Liberman et al., 2009; Reeves et al., 2012). We found that *dl; dl-dGFP/+* embryos have highly widened gradients (σ=0.219±0.009), with severe flat-top/mild double-peaked phenotypes (Fig. 4D and Fig. 5A,B). However,
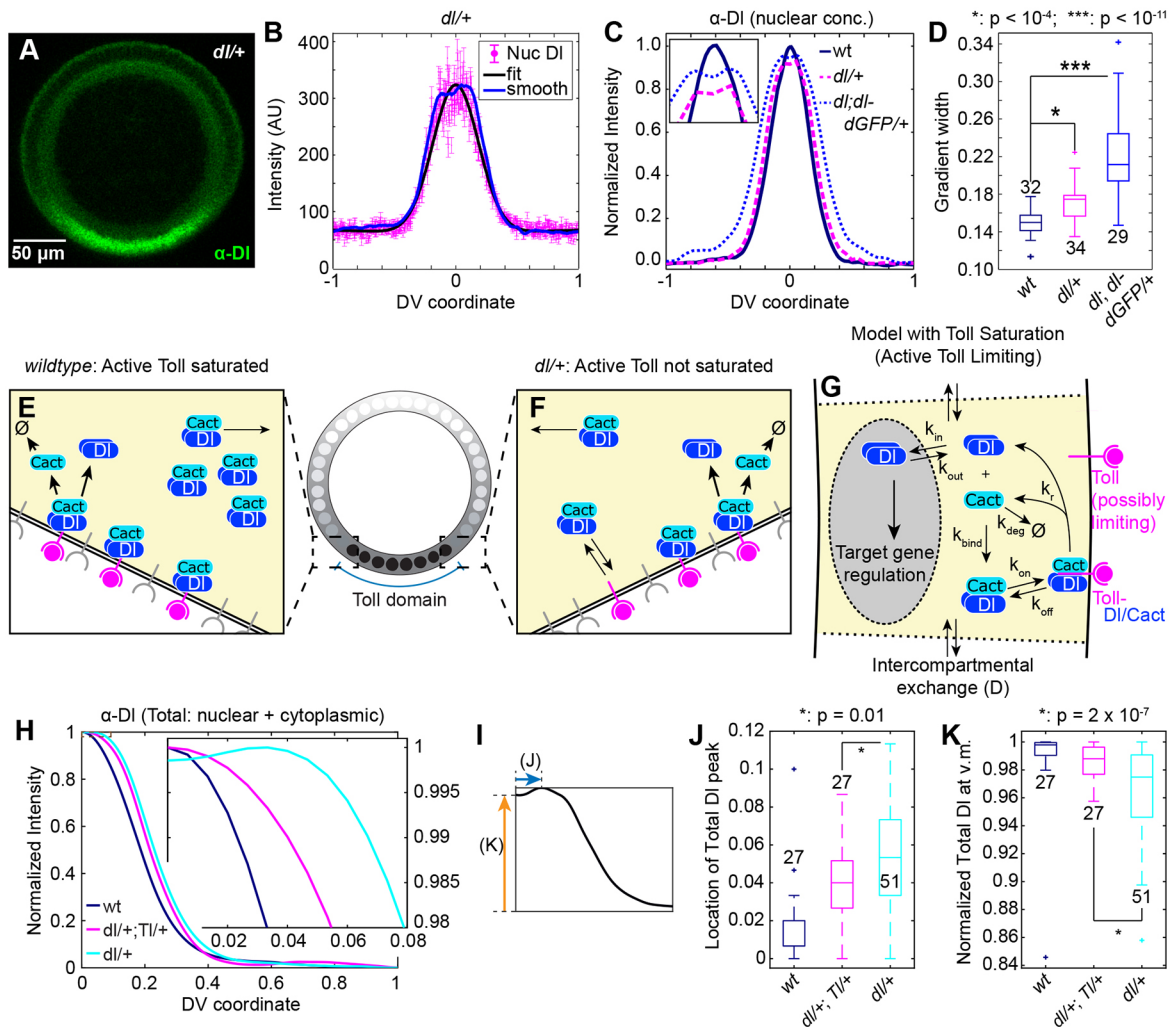
Fig. 4. Embryos from mothers heterozygous for Dl have a different-shaped Dl gradient that is explained by Toll saturation. (A) Cross section of an nc 14 embryo from a mother heterozygous for *dl* immunostained for Dl. (B) Plotted nuclear intensity of embryo in A as a function of DV coordinate (each magenta dot is one nucleus). Error bars indicate s.e.m. of nuclear intensity. Blue curve is the data of the individual nuclei smoothed by a sliding window of 50 nuclei; black curve is a fit of the data to a Gaussian. (C) Normalized average plots of the α-Dl nuclear fluorescence in wild-type, *dl/+* and *dl; dl-dGFP/+* embryos. Inset highlights differences in peak shape. (D) Box plot of gradient widths (σ) for the embryos in C. (E) Schematic of active Toll receptor saturation in wild-type embryos. In the edges of the Toll domain, Dl/Cact complexes can bypass active Toll receptors that are already bound by other Dl/Cact complexes. (F) Schematic of lack of active Toll saturation in *dl/+* embryos. Fewer Dl/Cact complexes can penetrate deep into the Toll domain. (G) Extended model of the Dl/Cact system in which active Toll receptors are saturable. (H) Normalized, average profiles of total α-Dl fluorescence in wild-type, *dl/+*; *Tl/+* and *dl/+* embryos. Inset reveals the difference in peak shape. The same color scheme and sets of embryos are presented in J and K. (I) Illustration of the variables compared in J and K. Blue arrow illustrates the distance from the ventral midline where the gradient peaks, and is compared across genotypes in J. Orange arrow illustrates the normalized value of the Dl gradient at the ventral midline, and is compared across genotypes in K. (J) Box plot of locations of total Dl peak (see blue arrow in I for embryos in H). (K) Box plot of normalized total Dl peak levels at the ventral midline (see orange arrow in I for embryos in H). See also Fig. S4.

it should be noted that σ is a less accurate measure of the width when the gradient is not bell shaped.

Because the peak shape is severely perturbed in *dl; dl-dGFP/+* embryos, we surmised that gene expression could be disrupted, which might explain why *dl; dl-dGFP/+* females are sterile. Therefore, we analyzed *sna* expression in *dl; dl-dGFP/+* embryos (*n*=33) and found that these embryos either lacked *sna* expression entirely (16/33), had *sna* expression too faint to quantify above background (5/33), or expressed *sna* in a very narrow domain (Figs 5B-E; Fig. S5), confirming our hypothesis that the double perturbation results in a breakdown of the typically robust patterning system. By contrast, embryos from *dl; dl-dGFP* mothers have normal *sna* expression (Fig. 5C,E), which shows that Dl-dGFP retains transcriptional function. Furthermore, embryos from *dl; dl-mVenus/+* mothers, which have a less severe shuttling defect than

dl; dl-dGFP/+ embryos, have robust *sna* expression (Fig. S5C,D) and are viable (our observations and Reeves et al., 2012). This result suggests that shuttling is indeed exacerbated in these embryos and that this shuttling defect is responsible for the female sterility.

Increasing the width of the active Toll domain results in a split peak of Dl

The shuttling hypothesis predicts that severe widening of the active Toll domain results in a split Dl gradient (Fig. S6A,B). As the extent of the Toll domain is controlled by Gurken/EGFR signaling during oogenesis (Sen et al., 1998; Schüpbach, 1987), we analyzed embryos from mothers carrying a hypomorphic EGFR allele (*Egfr[t1]*) (Roth and Schüpbach, 1994). We found that embryos from mothers heterozygous for this allele have significantly widened Dl gradients, and most (10/12) embryos from homozygous mothers have gradients
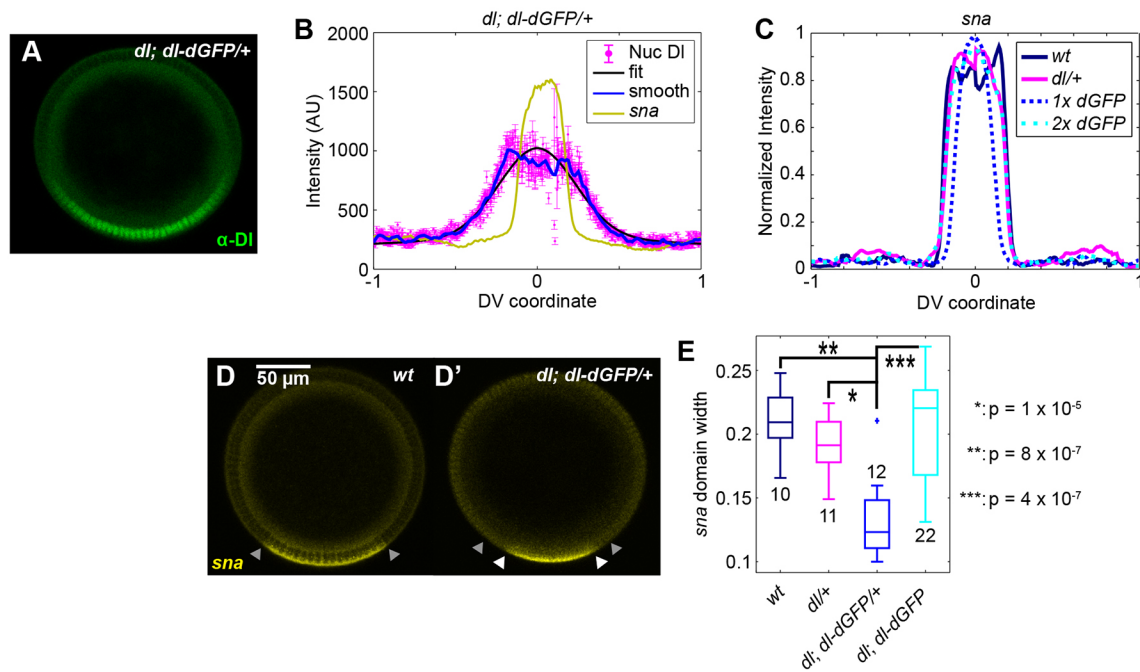
Fig. 5. Simultaneous perturbations to shuttling result in defects in the Dl gradient and in the *sna* domain. (A) Cross section of an nc 14 *dl; dl-dGFP/+* embryo immunostained for Dl. (B) Quantification of α-Dl nuclear fluorescence of the embryo in A. The *sna* domain is also shown (gold). (C) The average *sna* domain from embryos in Fig. 4C,D, plus *dl; dl-dGFP* embryos (labeled 1× dGFP). (D,D′) *sna* mRNA expression in wild type (D) and *dl; dl-dGFP/+* (D′). The embryo in D′ is the same embryo as in A and B. Arrowheads indicate width of *sna* domain in wild type (gray) and *dl; dl-dGFP/+* (white). (E) Box plot of *sna* domain widths for the embryos in C. *sna* domains in *dl; dl-dGFP* embryos are statistically narrower than those in other genotypes. See also Fig. S5.

so wide that the peak splits (Fig. 6A-D). This result is consistent with previous reports that various *gurken* and *Egfr* mutations generate a duplicated Dl gradient as measured by Dl staining, Twist staining, and sites of ventral furrow formation (Roth and Schüpbach, 1994), which are not readily explained in the absence of a shuttling phenomenon (Meinhardt, 2004; Moussian and Roth, 2005; Haskel-Ittah et al., 2012).

A model with Toll saturation predicts that the split peak can be alleviated either by decreasing the levels of active Toll receptors or by increasing the dosage of maternal *dl* (Fig. S6C-F). We chose to test the possibility by examining embryos from mothers carrying one (*Egfr[t1]; dl[RC]/+*) or two (*Egfr[t1]; dl[RC]*) extra copies of a Dl rescue construct (Reeves et al., 2012) in the *Egfr[t1]* background. These embryos have three or four copies of full-length Dl, respectively. We found that, as our model predicts, increasing the dosage of maternal *dl* reduces the severity of the split-peak phenotype (Fig. 6E; Fig. S6G-I), providing further evidence for active Toll receptor saturation.

An AP gradient of Dl supports the shuttling hypothesis

It has been suggested that a shuttling phenomenon also occurs through the processing of Spätzle (Spz), the ligand for Toll signaling (Haskel-Ittah et al., 2012), which might explain some of the phenotypes described here. To determine whether the hallmark phenotypes of shuttling could occur without assistance from the protease cascade or Spz processing, we expressed a constitutively active form of Toll (Toll[10b]) at the anterior pole of the developing embryo using the *bicoid* (*bcd*) 3′ UTR and the *bcd* promoter, similar to previously performed experiments using the stronger *Hsp83* promoter (Huang et al., 1997). Embryos from mothers carrying this construct (*bcd>Toll[10b]: bcd 3′ UTR*) have an AP Dl gradient in addition to the native DV gradient. Naïvely, one may expect that the existence of two gradients of active Toll signaling would result in higher concentrations of nuclear Dl where the two overlap. By

contrast, the shuttling hypothesis predicts that Dl nuclear concentration would be depleted in the region where both gradient tails overlap, as the two competing Dl/Cact sinks cause Cact to shuttle Dl toward both the anterior pole and the ventral midline (Fig. 7A-C). This prediction is borne out in experiments, as these embryos show a decreased intensity of the Dl gradient near the region of overlap. Furthermore, 64% (9/14) of these embryos show a visible narrowing of the *sna* expression domain at ~30% egg length, consistent with previously published data (Fig. 7B,C) (Huang et al., 1997). Our results show domain narrowing rather than a gap as previously reported, owing to the weaker *bcd* promoter.

Our modeling results further support that the shuttling mechanism is responsible for this phenomenon (Fig. 7C). We expanded our model system from a one-dimensional array of nuclear compartments to a two-dimensional array, and added a second Toll signaling domain perpendicular to the first (Supplementary Materials and Methods). Our simulation results show that the overlap between the AP and DV Toll domains creates a low point in nuclear Dl concentration, similar to our experimental results. We then approximated a threshold for *sna* expression based on the DV Dl gradient, and found that the local minimum in Dl concentration results in reduced or abolished *sna* expression in that region (Fig. 7C′).

We also examined embryos from mothers carrying a homozygous mutation in *gastrulation defective* (*gd[7]*), which eliminates the endogenous ventral-to-dorsal gradient. Swapping the *bcd* promoter for the stronger *Hsp83* promoter (*Hsp83>Toll[10b]: bcd 3′ UTR* construct; Huang et al., 1997), we were able to create a wider Dl gradient at the anterior pole. Half of these embryos (7/16) show two peaks of Dl (Fig. 7D-E); furthermore, they have a double peak of *sna* (Trisnadi et al., 2013). To determine whether this double-peak phenomenon was a result of the embryo's geometry at the pole, we analyzed embryos with an AP Dl gradient initiated by the weaker *bcd* promoter. These embryos showed no such double-

DEVELOPMENT
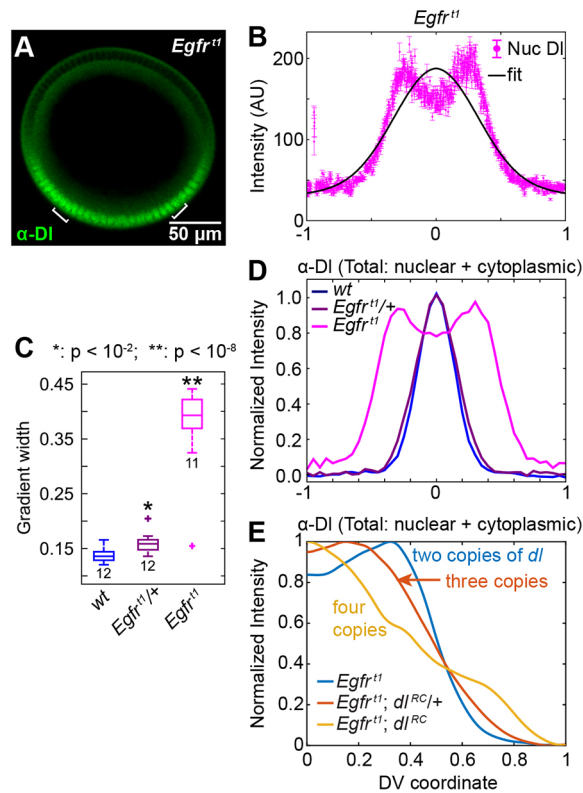
Fig. 6. The hypomorphic allele *Egfr^t1* significantly widens the Dl gradient.
(A) Cross section of an *Egfr^t1* embryo immunostained for Dl. Brackets indicate peaks of nuclear Dl. (B) Plotted α-Dl nuclear fluorescence of embryo in A as a function of DV coordinate (each pink dot is one nucleus). The shape has changed significantly from wild type, as the Gaussian curve (black) does not represent the gradient well. Error bars indicate s.e.m. of nuclear intensity. (C) Box plot of gradient widths (σ) for wild-type, *Egfr^t1*/+ and *Egfr^t1* embryos. Numbers indicate sample size. (D) Normalized average plot of total α-Dl fluorescence (nuclear+cytoplasmic) in the embryos in C, with the same color scheme. (E) Normalized total α-Dl fluorescence (nuclear+cytoplasmic) averaged from *Egfr^t1*, *Egfr^t1; dl^RC*/+ and *Egfr^t1; dl^RC*. See also Fig. S6.

peak effect (Fig. S7). These results further support our shuttling hypothesis as the Dl gradient progresses from narrow (weak promoter) to double peak (strong promoter), much as it does in the native DV system when the Toll domain expands.

DISCUSSION

In this study, we investigated the embryo-scale formation of the Dl morphogen gradient in the early *Drosophila* embryo. Based on our model and experimental verification, we conclude that establishment of peak levels of the Dl gradient is aided by a facilitated diffusion, or shuttling mechanism, in which Dl/Cact complex diffuses towards the ventral midline, where Cact is degraded. Lowering the diffusivity of either Dl or Cact widens the gradient rather than the narrowing that one might expect from a morphogen gradient established by (nonfacilitated) diffusion. The shuttling mechanism explains why Dl tagged with a weakly dimerizing GFP widens the gradient more than one tagged with monomeric GFP (Reeves et al., 2012), and also explains the related observation that one copy of Dl tagged with monomeric GFP variants complements loss of endogenous Dl while one copy of Dl-dGFP does not (Liberman et al., 2009; Reeves et al., 2012). Similarly, this mechanism makes sense of the observation that Dl tagged with β-galactosidase, which forms tetramers, is antimorphic (Govind et al., 1992), as the Dl moieties in tetramers of
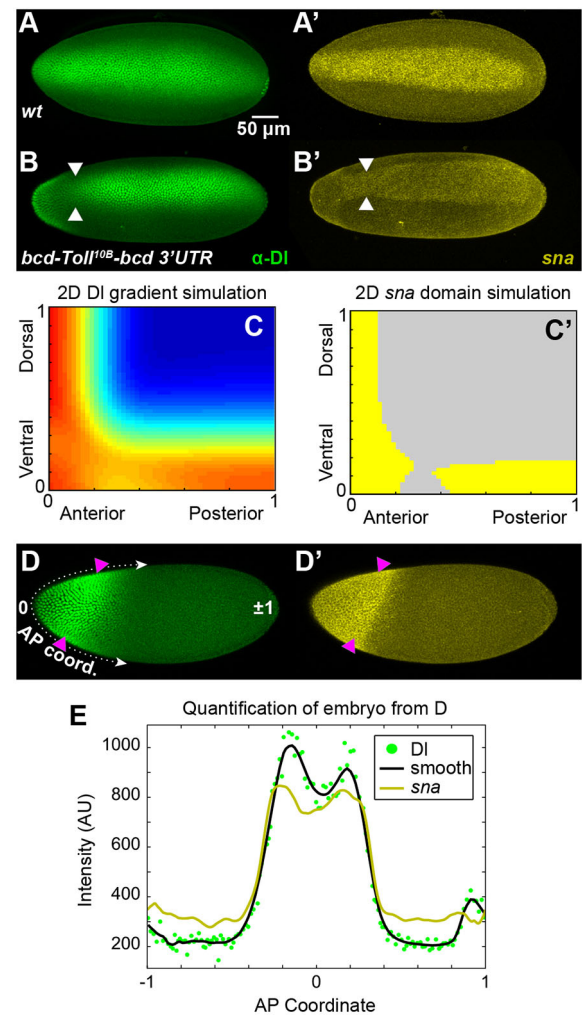
Fig. 7. An ectopic, AP dorsal gradient exhibits shuttling phenomena.
(A,A′) Dl and *sna* expression in a wild-type embryo. (B,B′) Dl and *sna* expression in an embryo with an AP gradient of Dl, driven by the *bcd* promoter in addition to the wild-type DV gradient. White arrowheads indicate a narrowing of each domain at ∼30% egg length. (C,C′) A 2D version of the model featuring AP and DV active Toll domains exhibiting a competing sink phenotype, in which a low point in the Dl gradient leads to a decrease in *sna* expression. (D,D′) Dl and *sna* expression in an embryo with an AP gradient of Dl, driven by the *Hsp83* promoter, and the DV gradient abolished by a homozygous mutation in *gd*. Magenta arrowheads show the second peak of expression; the peak is more clearly shown when the data are plotted in E. The definition of the AP coordinate for the plot in E is given, with 0 at the anterior pole, and ±1 at the posterior pole. (E) Plot of Dl and *sna* domains from the embryo in D. Each green dot is one nucleus and the black curve is a smoothing of the Dl data. Embryo images are maximal intensity projections. See also Fig. S7.

Dl-βgal dimerize with endogenous Dl to disrupt the formation of the endogenous Dl gradient.

When the Toll gradient is greatly expanded, as in embryos from *Egfr^t1* mothers (Roth and Schüpbach, 1994), the domains of saturated Toll receptors move further from the ventral midline, resulting in a split peak. This split-peak phenomenon has also been observed in the Dl gradient in abnormally large embryos (Garcia et al., 2013). This specific phenotype could be explained by the shuttling of the Toll ligand Spz (Haskel-Ittah et al., 2012); however, we observed the same phenomenon in embryos with an ectopic AP Dl gradient established by constitutively active Toll. In both cases, ventrally (anteriorly) diffusing Dl/Cact complex does not reach the

ventral midline (anterior pole) before being dissociated, leaving the ventral (anterior)-most nuclei somewhat devoid of Dl. A similar mechanism, in which the removal rate of BMP ligands surpasses the rate of BMP flux to the dorsal midline, has been suggested to explain the computationally predicted split-peak phenotype for the BMP system in the early embryo (Umulis et al., 2006).

We further propose that active Toll receptors are saturated in the edges of the Toll domain in wild-type embryos; this saturation is not essential to the shuttling mechanism per se, though it is necessary for the mechanism to explain phenotypes associated with changing the dose of maternal *dl*. Under wild-type conditions, a significant flux of Dl/Cact complex can bypass the saturated active Toll receptors in the edges of the Toll domain, which results in the accumulation of a smooth, intense peak of Dl signaling at the ventral midline of the embryo. However, in *dl*/+ embryos, there is not enough Dl/Cact complex to saturate active Toll receptors in the tails of the gradient, leading to less accumulation of Dl at the ventral midline (Liberman et al., 2009). We have verified this assumption of active Toll saturation in *dl*/+; *Tl*/+ and *Egfr*^{t1}; *dl*^{RC} embryos.

The shuttling mechanism requires four biophysical processes: (1) Dl binding to Cact; (2) Dl/Cact complex readily diffusing through the embryo; (3) Toll signaling acting as a sink for Dl/Cact complex; and (4) Cact protecting Dl from entering the nuclei. As our experiments with Dl-paGFP show that Dl does indeed move globally through the embryo, it is now clear that Dl/Cact shuttling naturally arises in the early embryo. Indeed, our previous Dl/Cact model (O'Connell and Reeves, 2015) did not explicitly have shuttling 'programmed in', but instead it was a natural consequence of the model equations. In the same way, shuttling naturally emerges in previous models of the Dl gradient without the authors' explicit intention (Ambrosi et al., 2014; Kanodia et al., 2009).

Given the natural emergence of the shuttling mechanism from the topology of the known Dl/Cact interactions, one may ask whether the mechanism operates at a relevant level in the fly embryo. In the Dpp system, formation of peak levels of Dpp signaling requires the BMP antagonist Sog, which binds to Dpp and facilitates its diffusion to the dorsal midline of the early embryo. Loss of zygotic Sog function results in loss of both the highest levels of Dpp signal as well as the expression of genes that require those peak levels (Ashe and Levine, 1999; Zusman et al., 1988; Rushlow et al., 2001). Cact serves as the analog to Sog in the Dl/Cact system. A seminal study of Cact showed that loss of Cact function results in an expansion of the domain of cells expressing *twi*, a gene that requires peak levels of nuclear Dl (Roth et al., 1991), suggesting that there is no need for shuttling of Dl through Cact to form the peak levels of the Dl gradient. By contrast, a recent quantitative study, which analyzed embryos with varying levels of compromised *cact* function, could support the possibility that shuttling is necessary for embryonic fitness (Cardoso et al., 2017). Embryos with stronger loss of *cact* function have progressively flatter Dl gradients with lower peak values and progressively narrower domains of *sna*, which, like *twi*, requires peak levels of Dl (Cardoso et al., 2017). Curiously, the same study suggests a third role for Cact in establishing the Dl gradient: Cact fragments that result from Toll-independent degradation potentiate Dl signaling, which might explain most, if not all, their *cact* mutant phenotypes. Even so, the authors maintain the position that the shuttling mechanism could be necessary for the formation of peak Dl levels. Further work should be done to continue to dissect novel roles Cact might have in Dl gradient formation.

Regardless of the conflicting data from *cact* mutant embryos, the data presented here from the *dl; dl-dGFP*/+ embryos show that, at minimum, the shuttling mechanism is required for formation of peak

levels of the Dl gradient (and the consequent *sna* expression) when Dl levels are compromised. Given the data presented here, the literature data explained by the shuttling hypothesis, and the fact that all biological processes required for shuttling are known to be present in the embryo, we suggest that Cact serves a dual role in establishing the Dl nuclear gradient: preventing nuclear translocation of Dl and shuttling of Dl.

MATERIALS AND METHODS
Fly lines
yw flies were used as wild type. *dl-paGFP*, *dl-mGFP* and *dl-dVenus* were created by BAC recombineering. For live imaging, flies carrying *dl-paGFP* were crossed to flies carrying H2A-RFP on the second chromosome (BS# 23651). *dl*/+ flies were created by cleaning up *dl*^{1} via two homologous recombinations with *yw* to generate *dl*^{1,2,5}. *cact*/+; *cact-full lacZ 25* flies were obtained from David Stein (Janelia Research Campus, Ashburn, VA, USA) (Fernandez et al., 2001). *dl-lacZ* flies were obtained from Govind et al. (1992). *dl-dGFP* and *dl-mVenus* flies and the original BACs used to create them were obtained from Angela Stathopoulos (California Institute of Technology, Pasadena, CA, USA). *dl-mGFP,dl*^{1,2,5} flies were created by homologous recombination. Presence of *dl-mGFP* was confirmed by w$^+$. Presence of *dl*^{1,2,5} was confirmed via sequencing by GENEWIZ. *Egfr*^{t1}/*CyO* flies were obtained from the Bloomington *Drosophila* Stock Center (# 2079). Flies carrying the *bcd>Toll*^{10b}: *bcd 3′ UTR* construct were obtained from Angela Stathopoulos. The plasmid carrying *FRT-stop-FRT Hsp83>Toll*^{10b}: *bcd 3′ UTR* was also obtained from Angela Stathopoulos. To remove the FRT-stop-FRT cassette, we crossed flies carrying this construct into a line carrying hsFLP on the X chromosome (BS# 8862). To remove the native DV Dl gradient, flies carrying the *Toll*^{10b}: *bcd 3′UTR* construct were crossed into a *gd*^{7} background. See Supplementary Materials and Methods for more details. *dl*/+; *Tl*/+ fly lines resulted from crossing the *dl*^{1,2,5}/+ fly line with *Tl*^{rv18}/+ (BS# 30913).

BAC recombineering
We followed Protocol 3 of the NCI at Frederick Recombineering website (http://ncifrederick.cancer.gov/research/brb/recombineeringinformation. aspx) to generate *dl-paGFP*, *dl-mGFP* and *dl-dVenus* in pACMAN (Venken et al., 2006). A proofreading Q5 DNA polymerase (New England Biolabs) was used to amplify sequences at a high level of authenticity. Using a GalK selection protocol (Warming et al., 2005), single amino acid mutations were introduced at residue 206 in previously established BACs (Reeves et al., 2012) to generate *dl-mGFP* (A206K) and *dl-dVenus* (K206A). *dl-paGFP* was created by adding the open reading frame of *paGFP* (Addgene plasmid #11911) (Patterson and Lippincott-Schwartz, 2002) in frame to the 3′ end of the *dl* open reading frame in a *dl* rescue construct (Reeves et al., 2012) in pACMAN (Venken et al., 2006) using a 6x-Gly linker. See Table S1 for a list of primers used.

Fluorescent *in situ* hybridization
All embryos were aged to 2-4 h, except for 'young' *yw* embryos, which were aged to 0-2 h, then fixed in 37% formaldehyde according to standard protocols (Kosman et al., 2004). A combination fluorescent *in situ* hybridization/fluorescent immunostaining was performed according to standard protocols (Kosman et al., 2004). Briefly, fixed embryos were washed in Tween/PBS buffer, then hybridized with a digoxigenin-conjugated anti-sense *sna* probe at 55°C overnight. The embryos were then washed and incubated with primary antibodies at 4°C overnight. Next, the embryos were washed and incubated for 1-2 h with fluorescent secondary antibodies at room temperature. The embryos were then washed and stored in 70% glycerol at −20°C. Embryos were imaged within one month of completing the protocol. See Supplementary Materials and Methods for more details, including suppliers and dilutions of antibodies.

Mounting and imaging of fixed samples
Embryos were cross-sectioned and mounted in 70% glycerol as described previously (Carrell and Reeves, 2015). Briefly, a razor blade was used to remove the anterior and posterior thirds of the embryo, leaving a cross

section ∼200 µm long by 200 µm in diameter. These sections were then oriented such that the cut sides became the top and bottom. They were imaged at 20× magnification on a Zeiss LSM 710 microscope. Fifteen z-slices 1.5 µm apart were analyzed. Embryos with an AP Dorsal gradient were mounted laterally in 70% glycerol using one piece of double-sided tape (weak *bcd* promoter) or two pieces of double-sided tape (strong *Hsp83* promoter). Images were taken at 2.5 µm intervals from just above the top of the embryo to the depth at which the embryo reached maximal size in the *xy* plane, which was assumed to be the midsagittal section. Stacks ranged from 15 to 25 slices.

Data analysis
Images of embryo cross sections were analyzed using previously derived code (Trisnadi et al., 2013). Briefly, the border of the embryo was found computationally, then the nuclei were segmented using a local thresholding protocol. The intensity of Dl in each segmented nucleus was calculated as the ratio between the intensity in the Dl channel divided by the intensity in the nuclear channel (Damle et al., 2006; Liberman et al., 2009). The intensity of mRNA expression and total Dl were calculated as average intensity within an annulus ∼18 µm wide around the perimeter of the embryo. A description of the image analysis of whole-mount embryos can be found in the Supplementary Materials and Methods and in Jermusyk et al. (2016).

All Dl gradients were fit to a Gaussian, and these fits were used to determine the width parameter, σ, and to normalize the Dl gradients. An r^2 goodness of fit was calculated for each embryo, and if this fell below 0.80, the measurement was discarded. Widths of *sna* domains were found by fitting the *sna* intensity curves to canonical profiles. For further explanation of these two procedures, see the Supplementary Materials and Methods. All replicates were biological.

Statistical significance was calculated using two-tailed homoscedastic *t*-tests. For 80% power, minimum sample size was calculated to be <10 embryos for our measurements of the Dl gradient width.

Activating paGFP in live embryos
Embryos were dechorionated by hand or for 30 s in 100% bleach. They were then mounted laterally on a slide coated with heptane glue. Deionized water was used as a mounting medium. Two pieces of double-sided tape were used to attach the coverslip. Images were taken using a 40× water immersion objective on an LSM 710 confocal microscope. Activation box: 9000 pixels (300×30 µm); number of activation passes (number of times the laser activates the region in a single cycle): 10; rest time (the length of rest time between cycles): 15 s; number of cycles: 40. Each activation session lasted ∼25 min and was followed by imaging the entire depth of the embryo. Each embryo underwent five activation sessions. Laser power was 3% for embryos activated near the ventral midline, and 2.5% for embryos activated near the dorsal midline. A 405 nm laser was used for activation and a 488 nm laser was used for excitation of the activated GFP.

Model of Dl/Cact interactions
In Figs 2 and 3, we used a simplified version of previously published models of Dl/Cact interactions to predict the effects of slowing diffusion (O'Connell and Reeves, 2015; Kanodia et al., 2009; Ambrosi et al., 2014). In brief, this model consists of four differential equations, representing nuclear and cytoplasmic Dl, and cytoplasmic Dl/Cact complex and Cact, respectively (Eqns 1-4; see also Fig. 2A for a schematic of the modeled processes).

$$\frac{\partial C_{\text{Dl},nuc}}{\partial t} = k_{in}C_{\text{Dl},cyt} - k_{out}C_{\text{Dl},nuc}, \tag{1}$$

$$\frac{\partial C_{\text{Dl},cyt}}{\partial t} = D_{\text{Dl}}\frac{\partial^2 C_{\text{Dl},cyt}}{\partial x^2} - k_{in}C_{\text{Dl},cyt} + k_{out}C_{\text{Dl},nuc} - k_{bind}C_{\text{Dl},cyt}C_{Cact}$$
$$+ k_{diss}(x)C_{DC}, \tag{2}$$

$$\frac{\partial C_{DC}}{\partial t} = D_{DC}\frac{\partial^2 C_{DC}}{\partial x^2} + k_{bind}C_{\text{Dl},cyt}C_{Cact} - k_{diss}(x)C_{DC}, \tag{3}$$

$$\frac{\partial C_{Cact}}{\partial t} = D_{Cact}\frac{\partial^2 C_{Cact}}{\partial x^2} + V_{cact} - k_{deg}C_{Cact} - k_{bind}C_{\text{Dl},cyt}C_{Cact}$$
$$+ k_{diss}(x)C_{DC}. \tag{4}$$

To simplify analysis and interpretation, we simulated 100 min of development with 51 nuclei positioned along a linear (*x*) axis and ignore mitosis and nuclear division. The active Toll gradient was modeled phenomenologically in space as $k_{diss}(x)=k_{diss,0}\exp(-0.5x^2/\phi^2)$ (Ambrosi et al., 2014; Kanodia et al., 2009; O'Connell and Reeves, 2015). In the Toll saturation model (Figs 4–7), activated Toll receptors were allowed to saturate (Fig. 4G), which altered the Dl/Cact complex dissociation term to a Michaelis–Menten-like saturable function (see Supplementary Materials and Methods). In other words, the final term in Eqns 2-4 became $k_{diss}C_{DC}/(K_R+C_{DC})$, where K_R is a Michaelis constant for Toll saturation. For more details on the model formulation, see Supplementary Materials and Methods.

To calculate flux of Dl-containing species, we applied Fick's law, which states that diffusive flux, *J*, which refers to the movement of a solute from areas of high concentration to areas of low concentration, occurs at a rate proportional to its concentration gradient, *dC/dx*, yielding $J=-DdC/dx$. The negative sign accounts for the fact that diffusive flux is in the direction of decreasing concentration, and *D* is the diffusion coefficient. By convention, we define our *x*-axis to be equal to 0 at the ventral midline and 1 at the dorsal midline (Fig. 2A); thus, a negative value for the flux indicates movement toward the ventral midline, and a positive value indicates movement toward the dorsal midline. Therefore, the calculation of flux of Dl-containing species (cytoplasmic Dl+Dl/Cact complex) is performed using the following equation:

$$J(x,t) = -D_{\text{Dl}}\frac{\partial C_{\text{Dl},cyt}}{\partial x} - D_{DC}\frac{\partial C_{DC}}{\partial x}. \tag{5}$$

Shuttling was defined as $J(x=0.33, t=100)<0$. This occurred when $D_{DC}/[D_{\text{Dl}}/K_{eq}]>1$, where $K_{eq}=k_{in}/k_{out}$ (see Fig. 2B).

To ensure our results were not the result of oversimplification, we also formulated a more complete (full) model of Dl/Cact/Toll interactions, which is an extension to the model found in O'Connell and Reeves (2015). This full model (see Supplementary Materials and Methods) consists of differential equations for three species distributed between two compartments: nuclear Dl, cytoplasmic Dl, nuclear Cact, cytoplasmic Cact, nuclear Dl/Cact complex, and cytoplasmic Dl/Cact complex, plus an equation for free active Toll receptor and one for active Toll receptor bound to Dl/Cact complex. It takes into account the mitosis and interphase associated with nc 10-14 and the possibility that Cact and Dl/Cact complex could be present in the nucleus. During mitosis, the nucleus becomes undefined, and the contents of each nucleus mix with those of the surrounding cytoplasm. At the end of mitosis, the nucleus reforms, and the concentration of Dl, Cact and Dl/Cact inside the nucleus is initialized as equal to their respective concentrations in the cytoplasm, and each species can enter and exit the nucleus. All cytoplasmic species can move between adjacent cytoplasmic compartments during interphase and mitosis.

The production rate of activated Toll receptors was modeled phenomenologically. The eight differential equations were nondimensionalized, resulting in a model with 20 free parameters. Optimization was performed in MATLAB (MathWorks) using an evolutionary optimization algorithm with stochastic ranking (Runarsson and Yao, 2000, 2005), yielding 114 parameter sets that were generally consistent with the spatiotemporal data published by Reeves et al. (2012). Further detail on model equations and analysis can be found in the Supplementary Materials and Methods.

We also analyzed two previous models of Dl/Cact interactions, which each have the processes necessary for shuttling, to investigate whether these processes together are sufficient for shuttling (Kanodia et al., 2009; Ambrosi et al., 2014). See Supplementary Materials and Methods for more details.

Data availability
All MATLAB files used for the model and data analysis are available from https:// github.ncsu.edu/ and additionally on the Reeves Lab website (people.engr.ncsu.edu/ gtreeves/). All image files are available from the Dryad Digital Repository (Carrell et al., 2017): doi:10.5061/dryad.4h00t.

Supplementary information
Supplementary information available online at
http://dev.biologists.org/lookup/doi/10.1242/dev.155549.supplemental

References
Ali-Murthy, Z. and Kornberg, T. B. (2016). Bicoid gradient formation and function in the Drosophila pre-syncytial blastoderm. *eLife* **5**, e13222.
Ambrosi, P., Chahda, J. S., Koslen, H. R., Chiel, H. J. and Mizutani, C. M. (2014). Modeling of the dorsal gradient across species reveals interaction between embryo morphology and toll signaling pathway during evolution. *PLoS Comput. Biol.* **10**, e1003807.
Ashe, H. L. and Levine, M. (1999). Local inhibition and long-range enhancement of Dpp signal transduction by Sog. *Nature* **398**, 427-431.
Belenkaya, T. Y., Han, C., Yan, D., Opoka, R. J., Khodoun, M., Liu, H. and Lin, X. (2004). Drosophila Dpp morphogen movement is independent of Dynamin-mediated endocytosis but regulated by the glypican members of heparan sulfate proteoglycans. *Cell* **119**, 231-244.
Belvin, M. P., Jin, Y. and Anderson, K. V. (1995). Cactus protein degradation mediates Drosophila dorsal-ventral signaling. *Genes Dev.* **9**, 783-793.
Ben-Zvi, D. Shilo, B.-Z., Fainsod, A. and Barkai, N. (2008). Scaling of the BMP activation gradient in Xenopus embryos. *Nature* **453**, 1205-1211.
Bergmann, A., Stein, D., Geisler, R., Hagenmaier, S., Schmid, B., Fernandez, N., Schnell, B. and Nüsslein-Volhard, C. (1996). A gradient of cytoplasmic Cactus degradation establishes the nuclear localization gradient of the dorsal morphogen in Drosophila. *Mech. Dev.* **60**, 109-123.
Cardoso, M. A., Fontenele, M., Lim, B., Bisch, P. M., Shvartsman, S. Y. and Araujo, H. M. (2017). A novel function for the IκB inhibitor Cactus in promoting Dorsal nuclear localization and activity in the Drosophila embryo. *Development* **144**, 2907-2913.
Carrell, S. N. and Reeves, G. T. (2015). Imaging the dorsal-ventral axis of live and fixed Drosophila melanogaster embryos. In *Tissue Morphogenesis. Methods in Molecular Biology* (ed. C. M. Nelson), pp. 63-78. New York: Springer.
Chopra, V. S. and Levine, M. (2009). Combinatorial patterning mechanisms in the Drosophila embryo. *Brief. Funct. Genomic. Proteomic.* **8**, 243-249.
Christian, J. L. (2012). Morphogen gradients in development: from form to function. *Wiley Interdiscip. Rev. Dev. Biol.* **1**, 3-15.
Damle, S., Hanser, B., Davidson, E. H. and Fraser, S. E. (2006). Confocal quantification of cis-regulatory reporter gene expression in living sea urchin. *Test* **299**, 543-550.
Delotto, R., Delotto, Y., Steward, R. and Lippincott-Schwartz, J. (2007). Nucleocytoplasmic shuttling mediates the dynamic maintenance of nuclear Dorsal levels during Drosophila embryogenesis. *Development* **134**, 4233-4241.
Dorfman, R. and Shilo, B. Z. (2001). Biphasic activation of the BMP pathway patterns the Drosophila embryonic dorsal region. *Development* **128**, 965-972.
Drier, E. A., Huang, L. H. and Steward, R. (1999). Nuclear import of the Drosophila Rel protein Dorsal is regulated by phosphorylation. *Genes Dev.* **13**, 556-568.
Drier, E. A., Govind, S. and Steward, R. (2000). Cactus-independent regulation of Dorsal nuclear import by the ventral signal. *Curr. Biol.* **10**, 23-26.
Driever, W. and Nüsslein-Volhard, C. (1988). A gradient of bicoid protein in Drosophila embryos. *Cell* **54**, 83-93.
Eldar, A., Dorfman, R., Weiss, D., Ashe, H., Shilo, B. Z. and Barkai, N. (2002). Robustness of the BMP morphogen gradient in Drosophila embryonic patterning. *Nature* **419**, 304-308.
Entchev, E. V., Schwabedissen, A. and González-Gaitán, M. A. (2000). Gradient formation of the TGF-β homolog Dpp. *Cell* **103**, 981-991.

Fahmy, K., Akber, M., Cai, X., Koul, A., Hayder, A. and Baumgartner, S. (2014). αTubulin 67C and Ncd are essential for establishing a cortical microtubular network and formation of the Bicoid mRNA gradient in Drosophila *PLoS ONE* **9**, e112053.
Fernandez, N. Q., Grosshans, J., Goltz, J. S. and Stein, D. (2001). Separable and redundant regulatory determinants in Cactus mediate its dorsal group dependent degradation. *Development* **128**, 2963-2974.
Garcia, M. Nahmad, M., Reeves, G. T. and Stathopoulos, A. (2013). Size-dependent regulation of dorsal–ventral patterning in the early Drosophila embryo. *Dev. Biol.* **381**, 286-299.
Govind, S., Whalen, A. M. and Steward, R. (1992). In vivo self-association of the Drosophila rel-protein dorsal. *Proc. Natl. Acad. Sci. USA* **89**, 7861-7865.
Govind, S., Drier, E., Huang, L. H. and Steward, R. (1996). Regulated nuclear import of the Drosophila rel protein dorsal: structure-function analysis. *Mol. Cell. Biol.* **16**, 1103-1114.
Gregor, T., Bialek, W., de Ruyter van Steveninck, R. R., Tank, D. W. and Wieschaus, E. F. (2005). Diffusion and scaling during early embryonic pattern formation. *Proc. Natl. Acad. Sci. USA* **102**, 18403-18407.
Gregor, T. Wieschaus, E. F., Mcgregor, A. P., Bialek, W. and Tank, D. W. (2007). Stability and nuclear dynamics of the Bicoid morphogen gradient. *Cell* **130**, 141-152.
Guerrero, I. and Kornberg, T. B. (2014). Hedgehog and its circuitous journey from producing to target cells. *Semin. Cell Dev. Biol.* **33**, 52-62.
Haskel-Ittah, M., Ben-Zvi, D., Branski-Arieli, M., Schejter, E. D., Shilo, B.-Z. and Barkai, N. (2012). Self-organized shuttling: generating sharp dorsoventral polarity in the early drosophila embryo. *Cell* **150**, 1016-1028.
Holley, S. A., Neul, J. L., Attisano, L., Wrana, J. L., Sasai, Y., O'connor, M. B., De Robertis, E. M. and Ferguson, E. L. (1996). The Xenopus dorsalizing factor noggin ventralizes Drosophila embryos by preventing DPP from activating its receptor. *Cell* **86**, 607-617.
Houchmandzadeh, B., Wieschaus, E. and Leibler, S. (2002). Establishment of developmental precision and proportions in the early Drosophila embryo. *Nature* **415**, 798-802.
Huang, A. M., Rusch, J. and Levine, M. (1997). An anteroposterior Dorsal gradient in the Drosophila embryo. *Genes Dev.* **11**, 1963-1973.
Isoda, K., Roth, S. and Nüsslein-Volhard, C. (1992). The functional domains of the Drosophila morphogen dorsal: evidence from the analysis of mutants. *Genes Dev.* **6**, 619-630.
Jermusyk, A. A., Murphy, N. P. and Reeves, G. T. (2016). Analyzing negative feedback using a synthetic gene network expressed in the Drosophila melanogaster embryo. *BMC Syst. Biol.* **10**, 85.
Kanodia, J. S., Rikhy, R., Kim, Y., Lund, V. K., Delotto, R., Lippincott-Schwartz, J. and Shvartsman, S. Y. (2009). Dynamics of the Dorsal morphogen gradient. *Proc. Natl. Acad. Sci. USA* **106**, 21707-21712.
Kosman, D., Mizutani, C. M., Lemons, D., Cox, W. G., McGinnis, W. and Bier, E. (2004). Multiplex detection of RNA expression in Drosophila embryos. *Science* **305**, 846.
Lander, A. D., Nie, Q. and Wan, F. Y. M. (2002). Do morphogen gradients arise by diffusion? *Dev. Cell* **2**, 785-796.
Liberman, L. M., Reeves, G. T. and Stathopoulos, A. (2009). Quantitative imaging of the Dorsal nuclear gradient reveals limitations to threshold-dependent patterning in Drosophila. *Proc. Natl. Acad. Sci. U.S.A.* **106**, 22317-22322.
Little, S. C., Tkačik, G., Kneeland, T. B., Wieschaus, E. F. and Gregor, T. (2011). The formation of the Bicoid morphogen gradient requires protein movement from anteriorly localized mRNA. *PLoS Biol.* **9**, e1000596.
Marqués, G., Musacchio, M., Shimell, M. J., Wünnenberg-Stapleton, K., Cho, K. W. Y. and O'connor, M. B. (1997). Production of a DPP activity gradient in the early Drosophila embryo through the opposing actions of the SOG and TLD proteins. *Cell* **91**, 417-426.
Matsuda, S., Harmansa, S. and Affolter, M., (2016). BMP morphogen gradients in flies. *Cytokine Growth Factor. Rev.* **27**, 119-127.
Meinhardt, H. (2004). Different strategies for midline formation in bilaterians. *Nat. Rev. Neurosci.* **5**, 502-510.
Mizutani, C. M., Nie, Q., Wan, F. Y. M., Zhang, Y.-T., Vilmos, P., Sousa-Neves, R., Bier, E., Marsh, J. L. and Lander, A. D. (2005). Formation of the BMP activity gradient in the drosophila embryo. *Dev. Cell* **8**, 915-924.
Moussian, B. and Roth, S. (2005). Dorsoventral axis formation in the Drosophila embryo–shaping and transducing a morphogen gradient. *Curr. Biol.* **15**, R887-R899.
Müller, P. Rogers, K. W., Yu, S. R., Brand, M. and Schier, A. F. (2013). Morphogen transport. *Development* **140**, 1621-1638.
O'Connell, M. D. and Reeves, G. T. (2015). The presence of nuclear cactus in the early Drosophila embryo may extend the dynamic range of the dorsal gradient *PLoS Comput. Biol.* **11**, e1004159.
Patterson, G. H. and Lippincott-Schwartz, J. (2002). A photoactivatable GFP for selective photolabeling of proteins and cells. *Science (New York, N.Y.)* **297**, 1873-1877.
Rahimi, N., Averbukh, I., Haskel-Ittah, M., Degani, N., Schejter, E. D., Barkai, N. and Shilo, B.-Z. (2016). A WntD-dependent integral feedback loop attenuates variability in drosophila toll signaling. *Dev. Cell* **36**, 401-414.

DEVELOPMENT

Reach, M., Galindo, R. L., Towb, P., Allen, J. L., Karin, M. and Wasserman, S. A. (1996). A gradient of cactus protein degradation establishes dorsoventral polarity in the Drosophila embryo. *Dev. Biol.* **180**, 353-364.

Reeves, G. T. and Stathopoulos, A. (2009). Graded dorsal and differential gene regulation in the Drosophila embryo. *Cold Spring Harb. Perspect Biol.* **1**, a000836.

Reeves, G. T., Trisnadi, N., Truong, T. V., Nahmad, M., Katz, S. and Stathopoulos, A. (2012). Dorsal-ventral gene expression in the Drosophila embryo reflects the dynamics and precision of the dorsal nuclear gradient. *Dev. cell,* **22**, 544-557.

Roth, S. and Schüpbach, T. (1994). The relationship between ovarian and embryonic dorsoventral patterning in Drosophila. *Development* **120**, 2245-2257.

Roth, S., Stein, D. and Nüsslein-Volhard, C. (1989). A gradient of nuclear localization of the dorsal protein determines dorsoventral pattern in the Drosophila embryo. *Cell* **59**, 1189-1202.

Roth, S., Hiromi, Y., Godt, D. and Nüsslein-Volhard, C. (1991). cactus, a maternal gene required for proper formation of the dorsoventral morphogen gradient in Drosophila embryos. *Development* **112**, 371-388.

Roy, S., Huang, H., Liu, S. and Kornberg, T. B. (2014). Cytoneme-mediated contact-dependent transport of the drosophila decapentaplegic signaling protein. *Science* **343**, 1244624.

Runarsson, T. P. and Yao, X. (2000). Stochastic ranking for constrained evolutionary optimization. *IEEE Trans. Evol. Comput.* **4**, 284-294.

Runarsson, T. P. and Yao, X. (2005). Search biases in constrained evolutionary optimization. *IEEE Trans. Syst. Man Cybern. C Appl. Rev.* **35**, 233-243.

Rushlow, C. A. and Shvartsman, S. Y. (2012). Temporal dynamics, spatial range, and transcriptional interpretation of the Dorsal morphogen gradient. *Curr. Opin. Genet. Dev.* **22**, 542-546.

Rushlow, C., Colosimo, P. F., Lin, M. C., Xu, M. and Kirov, N. (2001). Transcriptional regulation of the Drosophila gene zen by competing Smad and Brinker inputs. *Genes Dev.* **15**, 340-351.

Schüpbach, T. (1987). Germ line and soma cooperate during oogenesis to establish the dorsoventral pattern of egg shell and embryo in drosophila melanogaster. *Cell* **49**, 699-707.

Schwank, G., Dalessi, S., Yang, S. F., Yagi, R., de Lachapelle, A. M., Affolter, M., Bergmann, S. and Basler, K. (2011). Formation of the long range dpp morphogen gradient. *PLoS Biol.* **9**, e1001111.

Sen, J., Goltz, J. S., Stevens, L. and Stein, D. (1998). Spatially restricted expression of pipe in the drosophila egg chamber defines embryonic dorsal–ventral polarity. *Cell* **95**, 471-481.

Shilo, B.-Z. Haskel-Ittah, M., Ben-Zvi, D., Schejter, E. D. and Barkai, N. (2013). Creating gradients by morphogen shuttling. *Trends Genet.* **29**, 339-347.

Shimmi, O., Umulis, D., Othmer, H. and O'Connor, M. B. (2005). Facilitated transport of a Dpp/Scw heterodimer by Sog/Tsg leads to robust patterning of the drosophila blastoderm embryo. *Cell* **120**, 873-886.

Smith, J. C. (2009). Forming and interpreting gradients in the early Xenopus embryo. *Cold Spring Harbor Perspect. Biol.* **1**, a002477.

Spirov, A., Fahmy, K., Schneider, M., Frei, E., Noll, M. and Baumgartner, S. (2009). Formation of the bicoid morphogen gradient: an mRNA gradient dictates the protein gradient. *Development* **136**, 605-614.

Stathopoulos, A. and Levine, M. (2002). Dorsal gradient networks in the Drosophila embryo. *Dev. Biol.* **246**, 57-67.

Steward, R., Zusman, S. B., Huang, L. H. and Schedl, P. (1988). The dorsal protein is distributed in a gradient in early drosophila embryos. *Cell* **55**, 487-495.

Trisnadi, N., Altinok, A., Stathopoulos, A. and Reeves, G. T. (2013). Image analysis and empirical modeling of gene and protein expression. *Methods (San Diego, Calif.)* **62**, 68-78.

Umulis, D. M., Serpe, M., O'connor, M. B. and Othmer, H. G. (2006). Robust, bistable patterning of the dorsal surface of the Drosophila embryo. *Proc. Natl. Acad. Sci. USA* **103**, 11613-11618.

Venken, K. J. T., He, Y., Hoskins, R. A. and Bellen, H. J. (2006). P[acman]: a BAC transgenic platform for targeted insertion of large DNA fragments in D. melanogaster. *Science (New York, N.Y.)* **314**, 1747-1751.

Wang, Y.-C. and Ferguson, E. L. (2005). Spatial bistability of Dpp-receptor interactions during Drosophila dorsal-ventral patterning. *Nature* **434**, 229-234.

Warming, S., Costantino, N., Court, D. L., Jenkins, N. A. and Copeland, N. G. (2005). Simple and highly efficient BAC recombineering using galK selection. *Nucleic Acids Res.* **33**, e36.

Wartlick, O., Kicheva, A. and González-Gaitán, M. (2009). Morphogen gradient formation. *Spring* **1**, a001255.

Whalen, A. M. and Steward, R. (1993). Dissociation of the Dorsal-Cactus complex and phosphorylation of the Dorsal protein correlate with the nuclear localization of Dorsal. *J. Cell Biol.* **123**, 523-534.

Zacharias, D. A., Violin, J. D., Newton, A. C. and Tsien, R. Y. (2002). Partitioning of lipid-modified monomeric GFPs into membrane microdomains of live cells. *Science* **296**, 913-916.

Zusman, S. B., Sweeton, D. and Wieschaus, E. F. (1988). short gastrulation, a mutation causing delays in stage-specific cell shape changes during gastrulation in Drosophila melanogaster. *Dev. Biol.* **129**, 417-427.

DEVELOPMENT

Supplemental Materials and Methods

Analysis of the Simplified Model

Our simplified model begins as Eqs 1-4. The next step is to non-dimensionalize the equations by applying the following transformations:

$$n \equiv \frac{C_{Dl,nuc}}{C_{Dl}^0}, \qquad u \equiv \frac{C_{Dl,cyt}}{C_{Dl}^0}, \qquad w \equiv \frac{C_{DC}}{C_{Dl}^0}, \qquad v \equiv \frac{C_{cact}}{C_{cact}^0},$$

where C_{Dl}^0 is the initial concentration of Dl in the embryo, and $C_{cact}^0 \equiv V_{Cact}/k_{deg}$. After transforming the state variables into their non-dimesionalized forms in this manner, we arrive at the following equations:

$$\frac{\partial n}{\partial t} = \hat{k}_{in}u - \hat{k}_{out}n, \qquad (S1).$$

$$\frac{\partial u}{\partial t} = \hat{D}_{dl}\frac{\partial^2 u}{\partial x^2} - \hat{k}_{in}u + \hat{k}_{out}n - \hat{k}_{bind}uv + \hat{k}_{diss}(x)w, \qquad (S2).$$

$$\frac{\partial w}{\partial t} = \hat{D}_{DC}\frac{\partial^2 w}{\partial x^2} + \hat{k}_{bind}uv - \hat{k}_{diss}(x)w, \qquad (S3).$$

$$\tau_{Cact}\frac{\partial v}{\partial t} = \hat{D}_{Cact}\frac{\partial^2 v}{\partial x^2} + 1 - v - \mu(\hat{k}_{bind}uv - \hat{k}_{diss}(x)w), \qquad (S4).$$

In these equations, time is measured in minutes and space is measured in embryo DV axis lengths. Therefore, the following dimensionless constants appear in the equations:

$$\hat{k}_{in} \equiv k_{in}T, \qquad \hat{k}_{out} = k_{out}T, \qquad \hat{D}_{Dl} \equiv \frac{D_{Dl}T}{L^2}, \qquad \hat{D}_{DC} \equiv \frac{D_{DC}T}{L^2}, \qquad \hat{D}_{Cact} \equiv \frac{D_{Cact}}{k_{deg}L^2}$$

$$\hat{k}_{bind} \equiv k_{bind}C_{Cact}^0T, \qquad \hat{k}_{diss}(x) \equiv k_{diss}(x)T, \qquad \tau_{Cact} \equiv (k_{deg}T)^{-1}, \qquad \mu = \frac{C_{Dl}^0T}{C_{Cact}^0k_{deg}},$$

where $T = 1$ min and $L = 280$ μm (the length of the DV axis from ventral midline to dorsal midline).

These equations are simplified in the following manner. First, as Cact has a high turnover rate, we assume that τ_{Cact}, $\hat{D}_{cact}$, and μ are small compared to unity. This results in a spatially uniform, pseudo steady state for free Cact, or $v = 1$. Next, we assume that nuclear import and export are in pseudo equilibrium, so that $n \approx \hat{k}_{out}u/\hat{k}_{in}$, or $n \approx K_{eq}u$, where $K_{eq} \equiv k_{in}/k_{out}$ is the equilibrium constant for net nuclear import of Dl. If we then sum equations (S1) and (S2), we arrive at:

$$\frac{\partial}{\partial t}(u + K_{eq}u) = \hat{D}_{Dl}\frac{\partial^2 u}{\partial x^2} - \hat{k}_{bind}uv + \hat{k}_{diss}(x)w,$$

or,

$$\frac{\partial u}{\partial t} = \frac{1}{1 + K_{eq}}\left[\hat{D}_{Dl}\frac{\partial^2 u}{\partial x^2} - \hat{k}_{bind}u + \hat{k}_{diss}(x)w\right], \qquad (S5).$$

Note that v has dropped out of the equation. It should also be noted that the criterion for shuttling to occur in this model is now more clear. The ratio of $\hat{D}_{cact}$ must be greater than effective diffusivity in Eqn

S5, which is $\widehat{D}_{Dl}/(1 + K_{eq})$. Together, these two simplifications reduce our system to two differential equations, one for cytoplasmic Dl (u; Eq S5), and one for cytoplasmic Dl/Cact complex (w; Eq S3).

Formulation of Toll saturation term
According to Fig. 4G, the dissociation of Dl/Cact complex can be expressed in the following steps:

$$Dl/Cact + Toll \xrightleftharpoons[k_{off}]{k_{on}} [Toll - Dl/Cact] \xrightarrow{k_r} Dl + Cact + Toll.$$
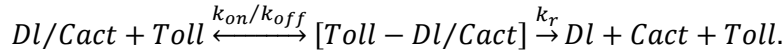
This reaction scheme is formally identical to the traditional Michaelis-Menten reaction scheme. In the case in which Toll levels are limiting (and roughly constant in total), if a pseudo steady state is assumed about the intermediate tripartite complex, the resulting expression for the rate of dissociation is:

$$r_{diss} = k_{diss}(x) \frac{w}{K_R + w},$$

where $K_R = (k_{off} + k_r)/k_{on}$ and $k_{diss} = k_r[Toll]_{tot}$, and $[Toll]_{Tot} = [Toll] + [Dl/Cact/Toll]$ (assumed roughly constant). Therefore, this Toll saturation regime replaces the final terms of Eqs S3 and S5 with

$$\widehat{k}_{diss}(x)w \to \widehat{k}_{diss}(x) \frac{w}{K_R + w}.$$

Random parameter screen
Parameters were varied randomly on a log space within reasonable constraints, and each parameter set was scored to determine whether shuttling was taking place. Both diffusivities were varied from 10^{-3} to 10^3 (see Parameter Estimation subsection), $\widehat{k}_{bind}$ was varied from 10^{-1} to 10^2, $\widehat{k}_{diss}$ was varied from 10^{-4} to 10^2, and K_R was varied from 10^{-2} to 10^2. The lower limit for $\widehat{k}_{bind}$ was higher than for other parameters because the strength of the Dl/Cact interaction needed to high enough to prevent Dl from entering the nuclei everywhere. The equilibrium constant was held fixed at $K_{eq} = 4$, which roughly reflects the ratio of nuclear to cytoplasmic Dl levels near the ventral midline, and ϕ was held fixed at 0.15, which roughly reflects the width of wildtype Dl gradients.

The metric to determine if a parameter set results in shuttling behavior is given in Eqn 5 in the Materials and Methods. Additionally, to score whether a parameter set results in widening of the gradient when diffusion is lowered, the same small fold-change perturbation was made to both diffusivities, and the width of the gradient was measured as the location where the gradient passes 60% max. If this width was higher than the width measured for the wildtype (non-diffusivity perturbed) gradient, then the parameter set was scored as positive for diffusion-based widening.

A parameter set was scored as positive for a split peak when the dosage of Dl was halved when the maximum of the gradient did not occur at $x = 0$, but did occur there for the wildtype (non-dosage perturbed) gradient. The same procedure was used for Toll-domain based peak splitting, for when ϕ was doubled.

Analysis of the Full Model

We also analyzed a more complete model of Dl/Cact interactions, which is an extension our previously-published mathematical model (O'Connell and Reeves, 2015). Here we explicitly account for both active Toll receptors and active Toll bound to Dl/Cact complex (Eqns S12 & S13, respectively) , which allows for the possibility that Toll activity is limiting. The full model of Dl/Cact/Toll interactions consists of a set of eight differential equations for each nucleus h (below). The equations describe the nuclear/cytoplasmic exchange of Dl, Cact and Dl/Cact complex, as well as the interactions between Dl, Cact, Dl/Cact complex and Toll receptors (see also Figs. 2A, 4G). The equations are simulated over nuclear cycles (NCs) 10-14 and for each nucleus $h = 1 \dots M_{NC}$, where M_{NC} is the number of nuclei in the given NC, as previously described (O'Connell & Reeves 2015). Thus, there are a total of $8M_{NC}$ equations during each nuclear cycle. By NC, $M_{10} = 13, M_{11} = 19, M_{12} = 26, M_{13} = 36, M_{14} = 51$.

$$V_n \frac{d}{dt}[Dl]_{nuc}^h = k_{in,Dl}A_n[Dl]_{cyt}^h - k_{out,Dl}A_n[Dl]_{nuc}^h - k_bV_n[Dl]_{nuc}^h[Cact]_{nuc}^h + k_dV_n[Dl/Cact]_{nuc}^h$$

(S6)

$$V_c\frac{d}{dt}[Dl]_{cyt}^h = k_{m,Dl}A_c\left([Dl]_{cyt}^{h-1} - 2[Dl]_{cyt}^h + [Dl]_{cyt}^{h+1}\right) + k_{Toll,2}A_{Toll}[Toll:Dl/Cact]^h$$
$$- k_{in,Dl}A_n[Dl]_{cyt}^h + k_{out,Dl}A_n[Dl]_{nuc}^h - k_bV_n[Dl]_{cyt}^h[Cact]_{cyt}^h + k_dV_n[Dl/Cact]_{cyt}^h$$

(S7)

$$V_n\frac{d}{dt}[dl/Cact]_{nuc}^h$$
$$= k_{in,dl/Cact}A_n[dl/Cact]_{cyt}^h - k_{out,dl/Cact}A_n[dl/Cact]_{nuc}^h + k_bV_n[dl]_{nuc}^h[Cact]_{nuc}^h$$
$$- k_dV_n[dl/Cact]_{nuc}^h$$

(S8)

$$V_c\frac{d}{dt}[Dl/Cact]_{cyt}^h$$
$$= k_{m,Dl/Cact}A_c\left([Dl/Cact]_{cyt}^{h-1} - 2[Dl/Cact]_{cyt}^h + [Dl/Cact]_{cyt}^{h+1}\right)$$
$$- k_{Toll,b}A_{Toll}[Toll]^h[Dl/Cact]_{cyt}^h + k_{Toll,1}A_{Toll}[Toll:Dl/Cact]^h$$
$$- k_{in,Dl/Cact}A_n[Dl/Cact]_{cyt}^h + k_{out,Dl/Cact}A_n[Dl/Cact]_{nuc}^h + k_bV_c[Dl]_{cyt}^h[Cact]_{cyt}^h$$
$$- k_dV_c[Dl/Cact]_{cyt}^h$$

(S9)

$$V_n\frac{d}{dt}[Cact]_{nuc}^h = k_{in,Cact}A_n[Cact]_{cyt}^h - k_{out,Cact}A_n[Cact]_{nuc}^h - k_bV_n[Dl]_{nuc}^h[Cact]_{nuc}^h$$
$$+ k_dV_n[Dl/Cact]_{nuc}^h$$

(S10)

$$V_c \frac{d}{dt}[Cact]_{cyt}^h = k_{m,Cact}A_c\left([Cact]_{cyt}^{h-1} - 2[Cact]_{cyt}^h + [Cact]_{cyt}^{h+1}\right) + k_{Toll,2}A_{Toll}[Toll:Dl/Cact]^h$$
$$- k_{in,Cact}A_n[Cact]_{cyt}^h + k_{out,Cact}A_n[Cact]_{nuc}^h - k_b V_c[Dl]_{cyt}^h[Cact]_{cyt}^h$$
$$+ k_d V_c[Dl/Cact]_{cyt}^h + P_{cact} - k_{deg}V_c[Cact]_{cyt}^h$$

$$(S11)$$

$$A_{Toll}\frac{d}{dt}[Toll]^h = (k_{Toll,1} + k_{Toll,2})A_{Toll}[Toll:Dl/Cact]^h - k_{Toll,b}\,A_{Toll}[Toll]^h[Dl/Cact]_{cyt}^h$$
$$+ k_{act}A_{Toll}\,f(x) - k_{deact}A_{Toll}[Toll]^h$$

$$(S12)$$

$$A_{Toll}\frac{d}{dt}[Toll:Dl/Cact]^h$$
$$= k_{Toll,b}A_{Toll}[Toll]^h[Dl/Cact]_{cyt}^h - (k_{Toll,1} + k_{Toll,2})A_{Toll}[Toll:Dl/Cact]^h$$

$$(S13)$$

Equation S6 describes the time evolution of the concentration of Dl in the nucleus. The first two terms on the right hand side (RHS) describe the import into and export from the nucleus, respectively, controlled by the rate constants k_{in} and k_{out}, respectively. The parameter A_n represents the surface area of the nucleus. The final two terms describe the binding and dissociation of Dl to/from Cact, controlled by the parameters k_b and k_d, respectively. The volume of the nucleus, which is where the binding/dissociation events occur, is represented by V_n, which is held fixed within a given nuclear cycle interphase, but can vary from nc to nc. Equation S7 describes the time evolution of the concentration of Dl in the cytoplasm, has similar terms as to those found in Equation S6, but also has a term that describes the intercompartmental transport (often referred to here as simply diffusion) of Dl, as well as a term that describes Toll-mediated dissociation of the Dl/Cact complex. The transport term consists of three factors. The first factor is the mass transfer coefficient, in µm/min, that describes the rate at which intercompartmental transport takes place. The second factor, A_c, is the area shared by neighboring compartments, which changes with each nuclear cycle. The third factor, $\left([Dl]_{cyt}^{h-1} - 2[Dl]_{cyt}^h + [Dl]_{cyt}^{h+1}\right) = \left([Dl]_{cyt}^{h-1} - [Dl]_{cyt}^h\right) + \left([Dl]_{cyt}^{h+1} - [Dl]_{cyt}^h\right)$, describes the concentration driving force for exchange between cytoplasmic compartments h and $h-1$ plus that for exchange between cytoplasmic compartments h and $h+1$. It should be noted that, if this factor is normalized by $(\Delta x)^2$, where Δx is the distance between two neighboring compartments, then this approximates the second derivative in space on a discretized mesh. The Toll term, $k_{Toll,2}A_{Toll}[Toll:Dl/Cact]$ is composed of three factors, the first being the rate constant describing the Toll-mediated dissociation of Dl/Cact complex, the second being the plasma membrane surface area available to the cytoplasmic compartment, and the last being the surface concentration of Dl/Cact complex bound to the cytoplasmic tail of the active Toll receptor signaling complex.

Equations S8 and S9 describe the time evolution of nuclear and cytoplasmic Dl/Cact complex, respectively. The second term on the RHS of Equation S9 describes the binding ($k_{Toll,b}$) of active Toll with cytoplasmic Dl/Cact complex, while the third term describes the dissociation (without reaction) of Dl/Cact complex from the active Toll receptor, which is controlled by the rate constant $k_{Toll,1}$.

Equations S10 and S11 describe the time evolution of nuclear and cytoplasmic Cact, respectively. The final two terms in Equation S11 describe the per-nucleus production rate of Cact and the Toll-signal-independent degradation of Cact, respectively.

The final two equations describe the time evolution of active Toll and active Toll bound to Dl/Cact complex, respectively. In Equation S12, the third term on the RHS represents the spatially-dependent production rate of active Toll receptors, which we model phenomenologically by the function $f(x)$ (see below). This phenomenology captures the rate at which free Spätzle (Spz), the ligand for Toll, binds to free Toll receptors. The final term represents the constitutive deactivation of active Toll receptors, and can be thought of the natural dissociation of Spz from Toll.

During interphase, all eight equations are used, and each cytoplasmic compartment contains a single nucleus; both the nucleus and the cytoplasmic compartment are assumed to be well-mixed. During mitosis, the nuclear species become undefined. At the interphase-to-mitosis transition, we assume the nuclear and cytoplasmic species become mixed, and thus, for a species with cytoplasmic concentration C and nuclear concentration N:

$$C_{mitosis} = \frac{V_c C_{interphase} + V_n N_{interphase}}{V_c + V_n}$$

…where V_c is the volume of the cytoplasm in the cytoplasmic compartment, and V_n is the volume of the nucleus.

At the mitosis-to-interphase transition, the number of cytoplasmic compartments increases. The cytoplasmic concentration is linearly interpolated in space to create the initial conditions for the next interphase in the new (greater number of) cytoplasmic compartments, as has been done previously (Kanodia et al., 2009; O'Connell and Reeves, 2015). We assume the nuclear concentration of each species is initially equal to the cytoplasmic concentration for each nucleus h.

The initial conditions for NC10 are zero for $[Dl]_{cyt}$, $[Dl]_{nuc}$, and $[Toll:Dl/Cact]$; C_{Dl}^0 for $[Dl/Cact]_{cyt}$ and $[Dl/Cact]_{nuc}$; C_{cact}^0 for $[Cact]_{cyt}$ and $[Cact]_{nuc}$; and $C_{Toll}^0 f(x)$ for $[Toll]$.

In the equations for the cytoplasmic species in cytoplasmic compartment $h = 1$, the intercompartmental exchange term becomes $k_m A_c (2C^{h+1} - 2C^h)$. Similarly, for $h = M_{NC}$, the term becomes $k_m A_c (2C^{h-1} - 2C^h)$. These changes are similar to no flux boundary conditions at both ends, representing the ventral and dorsal midlines.

Note that total Dl is conserved:

$$\frac{d}{dt}\left([Dl]_{cyt} + [Dl]_{nuc} + [Dl/Cact]_{cyt} + [Dl/Cact]_{nuc} + [Toll:Dl/Cact]\right) = 0$$

(9)

Toll receptors are activated by the ligand Spz on the ventral side of the embryo. We represent this by assuming active Toll receptors are produced with a Gaussian-like spatial dependence,

$$f(x) = \exp\left(-\frac{1}{2}\left(\frac{x}{\Phi}\right)^2\right)$$

(10)

where Φ is a measure of the width of the signaling domain (see Eqn S12). Peak production occurs at the ventral midline, located at $x = 0$. Active Toll receptors reversibly bind to Dl/Cact complexes to form Toll:Dl/Cact complex, which is consumed to produce Toll, free Dl and free Cact (rate constant $k_{Toll,2}$). The model equations were nondimensionalized, revealing a set of 20 free parameters:

$$\tilde{V}_n \frac{d}{d\tau} U^h_{nuc} = \zeta_{Dl}\tilde{A}_n U^h_{cyt} - \xi_{Dl}\tilde{A}_n U^h_{nuc} - \gamma\tilde{V}_n U^h_{nuc}Z^h_{nuc} + \beta_0\tilde{V}_n W^h_{nuc}$$

(S16)

$$\tilde{V}_c \frac{d}{d\tau} U^h_{cyt} = \lambda_U\tilde{A}_c\left(U^{h-1}_{cyt} - 2U^h_{cyt} + U^{h+1}_{cyt}\right) + \omega\epsilon\tilde{A}_{Toll}X^h - \zeta_{Dl}\tilde{A}_n U^h_{cyt} + \xi_{Dl}\tilde{A}_n U^h_{nuc} - \gamma\tilde{V}_c U^h_{cyt}Z^h_{cyt}$$
$$+ \beta_0\tilde{V}_c W^h_{cyt}$$

(S17)

$$\tilde{V}_n \frac{d}{d\tau} W^h_{nuc} = \zeta_{Dl-Cact}\tilde{A}_n W^h_{cyt} - \xi_{Dl-Cact}\tilde{A}_n W^h_{nuc} + \gamma\tilde{V}_n U^h_{nuc}Z^h_{nuc} - \beta_0\tilde{V}_n W^h_{nuc}$$

(S18)

$$\tilde{V}_c \frac{d}{d\tau} W^h_{cyt} = \lambda_W\tilde{A}_c\left(W^{h-1}_{cyt} - 2W^h_{cyt} + W^{h+1}_{cyt}\right) - \eta\epsilon\tilde{A}_{Toll}W^h_{cyt}Y^h + \nu\epsilon\tilde{A}_{Toll}X^h - \zeta_W\tilde{A}_n W^h_{cyt}$$
$$+ \xi_W\tilde{A}_n W^h_{nuc} + \gamma\tilde{V}_c U^h_{cyt}Z^h_{cyt} - \beta_0\tilde{V}_c W^h_{cyt}$$

(S19)

$$\tilde{V}_n \frac{d}{d\tau} Z^h_{nuc} = \zeta_Z\tilde{A}_n Z^h_{cyt} - \xi_Z\tilde{A}_n Z^h_{nuc} - \gamma\psi\tilde{V}_n U^h_{nuc}Z^h_{nuc} + \beta_0\psi\tilde{V}_n W^h_{nuc}$$

(S20)

$$\tilde{V}_c \frac{d}{d\tau} Z^h_{cyt} = \lambda_V\tilde{A}_c\left(Z^{h-1}_{cyt} - 2Z^h_{cyt} + Z^{h+1}_{cyt}\right) + \omega\epsilon\psi\tilde{A}_{Toll}X^h - \zeta_Z\tilde{A}_n Z^h_{cyt} + \xi_Z\tilde{A}_n Z^h_{nuc} - \gamma\psi\tilde{V}_c U^h_{cyt}Z^h_{cyt}$$
$$+ \beta_0\psi\tilde{V}_c W^h_{cyt} + 1 - \alpha\,\tilde{V}_c Z^h_{cyt}$$

(S21)

$$\frac{d}{d\tau} Y^h = (\nu + \omega)X^h - \eta\,Y^h W^h_{cyt} + \beta\,g(z) - \rho Y^h$$

(S22)

$$\frac{d}{d\tau} X^h = \eta Y^h W^h_{cyt} - (\nu + \omega)X^h$$

(S23)

$$U = \frac{[Dl]}{C^0_{Dl}}, Z = \frac{[Cact]}{C^0_{Cact}}, W = \frac{[Dl/Cact]}{C^0_{Dl}}, X = \frac{[Toll:Dl/Cact]}{C^0_{Toll}}, Y = \frac{[Toll]}{C^0_{Toll}}$$
$$\tilde{A}_n = \frac{A_n}{A^{14}_n}, \tilde{A}_{Toll} = \frac{A_{Toll}}{A^{14}_n}, \tilde{A}_c = \frac{A_c}{A^{14}_n}, \tilde{V}_n = \frac{V_n}{V^{14}_n}, \tilde{V}_c = \frac{V_c}{V^{14}_n}, \tau = \frac{t}{T}, z = \frac{x}{L}$$

$$\zeta_i = \frac{A_n^{14}k_{in,i}T}{V_n^{14}}, \xi_i = \frac{A_n^{14}k_{out,i}T}{V_n^{14}}, \lambda_i = \frac{k_{m,i}A_n^{14}T}{V_n^{14}}, \beta = \frac{k_{act}T}{C_{Toll}^0}, \epsilon = \frac{C_{Toll}^0 A_n^{14}}{C_{dl}^0 V_n^{14}}, \psi = \frac{C_{dl}^0}{C_{Cact}^0}, \alpha = k_{deg}T$$

$$g(z) = \exp\left(-\frac{z^2}{2\phi^2}\right), \phi = \frac{\Phi}{L}, \gamma = k_b C_{Cact}^0 T, \beta_0 = k_d T,$$

$$\nu = k_{Toll,1}T, \omega = k_{Toll,2}T, \eta = k_{Toll,b}C_{Dl}^0 T, \rho = k_{deact}T$$

…where C_i^0 are the initial concentrations of species i at nc 10, A_n^{14} is the surface area of the nucleus during nc 14, V_n^{14} is the volume of the nucleus during nc 14, L is the half-circumference of the embryo at 50% AP position (roughly equal to 280 µm), and $T = 1\ min$. It should be noted that C_{cact}^0 is set to be $P_{cact}T/V_n^{14}$.

In the scaled equations, initial conditions for NC10 are zero for U_{cyt}, U_{nuc}, and X; unity for $W_{cyt}, W_{nuc}, Z_{cyt}$, and Z_{nuc}; and $g(z)$ for Y. When perturbing dosages of *dl* or *Toll*, these initial conditions are scaled accordingly. For example, in *dl* heterozygotes, the initial conditions for W_{cyt} and W_{nuc} are 0.5. Additionally, in Toll heterozygotes, β is also halved.

The model was then made consistent with the dynamics of the system as published by Reeves et al. (2012). We used the Improved Stochastic Ranking Evolution Strategy (ISRES) algorithm from Thomas Philip Runarsson (downloaded from https://notendur.hi.is/tpr/index.php?page=software/sres/sres) (Runarsson and Yao, 2000, 2005) for optimization, which proceeded by the least squares error combined with penalty functions designed to reject parameter sets in which the Dl gradient width decreased upon halving the dosage. Optimization runs also incorporated a penalty function designed to reject parameter sets where nuclear Dl and Dl/Cact complex displayed reversed roles (i.e. Dl/Cact forming the ventral-to-dorsal gradient), as the algorithm is otherwise blind to the differences between the two species. In other words, if we included additional information in the error calculation, such as Dl-mediated gene expression (which depends on Dl but not Dl/Cact), these parameter sets would be rejected as a matter of course, but instead we chose to simply reject results known to be unrealistic via penalty function. The 2-D version of the model used to investigate competing AP and DV Toll domains (Figure 6) uses the same equations as above, except that intercompartmental exchange can happen along two axes. The system is modeled as a rectangular array of compartments (instead of a linear array), using a 5-point stencil to discretize the Laplacian as a central difference, with reflective boundary conditions along the perimeter. For simplicity, the number of compartments along each axis is held constant, as is the distance between them (Δx & Δy).

Relationship between intercompartmental exchange, flux, and diffusion
As mentioned above, intercompartmental exchange can be viewed as a coarse-grained diffusion term. For cytoplasmic species C, the intercompartmental exchange term centered at nucleus h is

$$k_m A_c\left(C^{h-1} - 2C^h + C^{h+1}\right)$$

If we multiply and divide by $(\Delta x)^2$, and also divide by the volume of the cytoplasm, this term becomes equal to:

$$\frac{k_m A_c(\Delta x)^2}{V_c}\frac{C^{h-1} - 2C^h + C^{h+1}}{(\Delta x)^2} \approx \frac{k_m A_c(\Delta x)^2}{V_c}\frac{d^2 C}{dx^2}$$

Thus, the effective diffusivity is $D_{eff} = k_m A_c(\Delta x)^2/V_c$.

In terms of the scaled equations, the intercompartmental exchange term is:

$$\lambda \tilde{A}_c\left(c^{h-1} - 2c^h + c^{h+1}\right)$$

…where c is the scaled version of the cytoplasmic species concentration, C. Recall that λ is defined as $k_m A_n^{14} T/V_n^{14}$, so that $\lambda \tilde{A}_c = D_{eff} \tilde{V}_c T/(\Delta x)^2$. If we define the scaled effective diffusivity as

$$\widehat{D}_{eff} = \frac{D_{eff} T}{L^2} = \frac{k_m A_c T (\Delta z)^2}{V_c} = \lambda \frac{\tilde{A}_c (\Delta z)^2}{\tilde{V}_c}$$

…then the scaled intercompartmental exchange term becomes:

$$\tilde{V}_c \widehat{D}_{eff} \frac{(c^{h-1} - 2c^h + c^{h+1})}{(\Delta z)^2} \approx \tilde{V}_c \widehat{D}_{eff} \frac{d^2 c}{dz^2}$$

Note that while k_m and λ are fixed parameters within a single simulation, D_{eff} and $\widehat{D}_{eff}$ vary with nuclear cycle.

Given these relationships, we can derive the relationship between approximate diffusive flux and intercompartmental transport:

$$\text{effective flux} = -\widehat{D}_{eff} \frac{dc}{dz} \approx -\widehat{D}_{eff} \frac{\Delta c}{\Delta z} = -\lambda \frac{\tilde{A}_c (\Delta z)^2}{\tilde{V}_c} \frac{\Delta c}{\Delta z}$$

…where $\Delta c = c^{h+1} - c^h$.

The "fluxes" plotted in Fig S2 are not actual fluxes. Instead, for species i, we plotted

$$\text{plotted flux} = -\lambda_i \frac{\Delta c_i}{\Delta z}$$

The remaining factors in the effective flux that are not included in the calculations are $\tilde{A}_c (\Delta z)^2 / \tilde{V}_c$, which are not species-specific (but they do change with nuclear-cycle). Thus, as we are comparing the plotted fluxes of two species within the same nuclear cycle, the plots are each proportional to their respective effective fluxes with the same proportionality constant.

Analysis of Kanodia and Ambrosi models
We recreated the model published by Kanodia et al. (2009) and the subsequent analysis performed by Ambrosi et al. (2014). As published, the Kanodia model assumes an equal rate of diffusion for Dl, Cact and Dl/Cact. However, to test the contribution of diffusion for each of the three species, we relax this assumption. Otherwise, the model remains unchanged for our analysis.

We used the parameter values published in Table 1, column 7 of Ambrosi et al. (2014) as the basis for a perturbation analysis. We chose this parameter set, termed "gyn 1" by the authors, because it is simulated in Figure 5C of Ambrosi et al., and in that scenario, it is shown that lowering the diffusivity widens the Dl gradient (as expected of a shuttling system). By perturbing the diffusion coefficients of this parameter set, we reproduce this widening phenomenon and show that, in the Kanodia/Ambrosi model, the widening is due to shuttling, as a decrease in the diffusion rate of Dl causes the gradient to contract ventrally, and a decrease in the diffusion of Dl/Cact causes the gradient to expand dorsally (Figure S2). In other words, shuttling is a property of this model, even when the authors did not intend it to be, and is not solely a property of our more detailed model. This is because shuttling arises naturally from the topology of a system that has a binder that, when in complex, can diffuse, protects the active species from capture, and dissociates from the active species in a spatially-dependent manner.

We also performed simulations of *dl* heterozygous embryos using the Ambrosi model (Figure S4C,D). In the paper (Ambrosi et al., 2014), the authors note that the normalized Dl gradient shape is independent

of the initial dose of Dl. The authors then suggest a possible mechanism for the widening (but not flat-top or double-peaked) phenotype of *dl/+* embryos. Namely, that in these embryos, the rate constant describing the Toll signal-independent degradation of free Cact protein by the proteasome increases four-fold in *dl/+* embryos. Therefore, their base parameter set is used to simulate wildtype embryos, and the alternative parameter set (with a four-fold increase in k_{Deg}) is used to simulate *dl/+* embryos. This results in a widening of the Dl gradient in *dl/+* embryos. However, when we compare simulations of wildtype vs. *dl/+* embryos using just the base parameter set (Table 1, Column 2 from Ambrosi et al., 2014) the normalized gradients collapse on each other (Figure S4D). Similarly, when we compare simulations of wildtype vs. *dl/+* embryos using just the alternative parameter set (Table 1, Column 3 from Ambrosi et al., 2014), the normalized gradients also collapse on each other (Figure S4D). In comparison, our model using explicit active Toll receptors reproduces the *dl/+* phenotype simply by reducing the dosage of *dl* (Figure S5EF), and does not require assuming that any other rate constants in the model change when the dosage of *dl* changes.

Fly lines
dl-paGFP was injected into the fly line yw; VK33 (landing site: third chromosome 65B2) by Duke University Model Systems, Durham, NC. *dl-dGFP* was inserted on the second chromosome at landing site attP40 by Genetic Services, Inc, Sudbury, MA. The *dl-dVenus* BAC was injected into the fly line yw; VK33 (landing site: third chromosome 65B2) by Genetic Services, Inc, Sudbury, MA.

The plasmid carrying *FRT-stop-FRT hsp83> Toll 10b: bcd 3'UTR* was injected into fly line attP2 with a landing site at (3L) 68A4 by Genetivision, Inc. (Houston, TX). To remove the FRT-stop-FRT cassette, we crossed male flies carrying this construct to virgins carrying hsFLP on both X chromosomes (BS# 8862). Females were allowed to lay embryos for 2-3 days before they were removed to a new vial. Vials containing 3-5 day old larvae (F1 generation) were heat shocked at 37°C for 2 hours. Males with red eyes (F1 generation) were crossed to virgin yw flies. Flies from the F2 generation were crossed to virgin yw flies to create the F3 generation, which was screened for female sterility, used as an indication of removal of the FRT-stop-FRT cassette.

In order to ablate the native DV Dl gradient, we generated a *gd⁷* line null for white. *gd⁷/FM3* flies (BS# 3109) were crossed to *yw* and the progeny crossed into stable lines that were screened for white eyes and females that were homozygous sterile. These flies (*gd⁷w⁻/FM3*) were then crossed to males carrying *toll¹⁰ᵇ: bcd 3'UTR/+* (weak *bcd* promoter construct on the second chromosome, strong *hsp83* promoter on the third chromosome). Males from this cross with the phenotype *gd⁷/Y; toll¹⁰ᵇ: bcd 3'UTR/+* were crossed again to *gd⁷w⁻/FM3* virgins, generating females that are homozygous null for *gd* (thus abolishing the wt Dl gradient) and provide their embryos with only the AP Dl gradient. We screened these females for the absence of bar (present on FM3) and the presence of *white* (present on *toll¹⁰ᵇ: bcd 3'UTR*).

In Fig. S3B,C, we evaluated the effect of a *dl-lacZ* transgene on the Dl gradient (Govind et al., 1992). As β-galactosidase (β-gal) tetramerizes, this fusion should slow diffusion of Dl to a greater extent than dGFP. Due to its anti-morphic nature (Govind et al., 1992), *dl-lacZ* is suspected to be expressed at low levels in surviving fly lines (Govind et al., 1996). Therefore, two copies of this transgene in a *dl/+* background were analyzed (Fig. S3B,C).

The *cact-lacZ* transgene studied in Fig. S3B,C was present in single copy and was in a heterozygous *cact* background (Fernandez et al., 2001).

Collection of Egfr^{t1}; dl^{RC} embryos
As shown in Figure S5H,I, only 3 and 1 embryos were imaged for the *Egfr^{t1}; dl^{RC}/+* and *Egfr^{t1}; dl^{RC}* fly lines, respectively. This resulted from multiple problems. First, there was a limited quantity of females found with the correct genotype. The females were collected from the *Egfr^{t1}/+; dl^{RC}/+* fly line. The relative lack of fitness of the *Egfr^{t1}; dl^{RC}/+* and *Egfr^{t1}; dl^{RC}* adults resulted in roughly ~10 such females found over the span of two weeks of collection from multiple bottles. Second, the fecundity of these females was severely compromised. Embryos were collected and fixed over 24 hour periods. The grape juice agar plates were checked for embryos every two hours. If any embryos were found, they were aged for two hours and fixed. Third, high attrition rates during fixation, especially during the devitellinization step, were observed (Kosman et al., 2004). Finally, upon imaging, most embryos were not found to be in the midst of nc 14. All of these factors contributed to the low sample size.

BAC Recombineering
Please note that residue 206 in GFP is actually residue 207 in the Venus protein as Venus has a Valine residue after the initial Methionine that is not present in the original GFP protein. For consistency, researchers refer to these residues by their location in GFP.

Fluorescent in situ *Hybridization*
Both *sna*-biotin and *sna*-fluorescein anti-sense RNA probes were used. Antibodies used were anti-dorsal 7A4 (deposited to the DSHB by Ruth Steward (DSHB Hybridoma Product anti-dorsal 7A4)) (1:10), donkey anti-mouse- 488 (Invitrogen A21202, Lot 81493) (1:500), rabbit anti-histone (abcam ab1791, Lot 940487) (1:5000), donkey anti-rabbit-546 (Invitrogen A10040, Lot 107388) (1:500), goat anti-biotin (ImmunoReagents, Raleigh, NC, GtxOt-070-D, Lot 19-19-112311) (1:50,000), donkey anti-goat-647 (Invitrogen A21447, Lot 774898) ((1:500), goat anti-fluorescein (Rockland 600-101-096, Lot 19458) (1:500), rabbit anti-fluorescein (Life Technologies A889, Lot 1458646) (1:500), goat anti-histone (Abcam, ab12079, Lots GR6952-4 and GR129411-1) (1:100)

Sequencing dl^{1.2.5}
Genomic DNA was extracted from males homozygous for *dl^{1.2.5}* according to standard protocols. We PCR amplified the entire *dl* region, then used 9 different primers to ensure complete sequencing coverage. Sequencing was performed by GENEWIZ, RTP, NC. The resulting sequence was compared to the consensus sequence available at FlyBase. Each mismatched codon was investigated as a potential source of an altered or truncated sequence. We found that a mutation at nt 3256 (entire *dl* genomic sequence) from G->T results in a premature stop codon, which we presume is the source of the amorphic allele.

Image analysis of toll^{10b}: bcd 3'UTRembryos
The Dorsal gradient and *snail* expression in embryos from mothers carrying the *toll^{10b}: bcd 3'UTR* transgene and homozygous for the *gd^7* mutation were analyzed using the following procedures. First, the z-stack images (taken as described in Experimental Procedures) were background subtracted assuming the mode of the image corresponded to zero fluorescence levels. Next, a maximum intensity projection was created, and the intensities from the three color channels (Dl, histone h3, and *snail*) were summed. The resulting image was Gaussian filtered in both the x and y directions using ten pixels as a kernel. This created an image I1 with the embryo as a single, bright object to facilitate discovery of the embryo boundary.

The embryo boundary was found according to (Jermusyk et al., 2016).

Once the boundary was found, an inner boundary was constructed by moving the 60 updated boundary points inward by 30 pixels in the direction of the local normal. This defined 60 quadrilaterals that encompass the outer periphery of the embryo. These quadrilaterals were laid on top of the image slice corresponding to the mid sagittal plane of the embryo, and each of the three color channels were unrolled using a affine transformation on the 60 quadrilaterals to result in 60 rectangles (see (Liberman et al., 2009; Trisnadi et al., 2013) for more information).

The nuclear channel was then segmented using a local thresholding (Trisnadi et al., 2013). The Dorsal intensity in each nucleus was then computed as the intensity in the Dorsal channel, normalized by the intensity in the nuclear channel. The intensity of *sna* expression was found as the average intensity of the *sna* channel within this unrolled strip loosely bounded by the nuclei.

Photobleaching experiments
Embryos were dechorionated, mounted, and imaged using the same protocol as described in the "Activating paGFP in Live Embryos" section. Individual nuclei were chosen at random across the embryo. Bleaching box: ~700 pixels (26.46 microns by 26.46 microns), bleaching time (amount of time the laser bleached the nuclei): ~20 seconds, number of cycles: 30. Each bleaching session lasted about 30 minutes (Movie S3) and was followed by imaging the entire depth of the embryo. Two nuclei per embryo were imaged in a single session. Laser power: 50% for each nucleus. A 488 nm laser was used for the bleaching of GFP.

Each FRAP experiment was analyzed according to the following procedure. First, the image sequence was stabilized using a standard optical flow protocol, which was necessary because the embryo sometimes moved very slightly during imaging. The optical flow protocol is as follows. In any xy frame at time point t, let the brightness at any pixel with coordinates x, y be $f(x, y, t)$. The goal is to find the values of dx and dy that make $f(x + dx, y + dy, t + dt) \approx f(x, y, t)$, where dt is the time difference between two successive frames. In a general optical flow protocol, there will be a different set of dx, dy depending on which pixel (or local pixel region) you are examining. However, for our particular application, we assume that the entire frame is translocating with the same dx and dy; that is, all nuclei move together as a rigid body. We also assume object brightness is roughly constant from frame to frame, save possibly a small average difference between two successive frames, df.

Performing a first order Taylor series expansion of f about (x, y, t), we obtain,
$$f(x + dx, y + dy, t + dt) = f(x, y, t) + f_x dx + f_y dy + f_t dt$$
…where f_x is the partial derivative of f in the x direction evaluated at pixel (x, y) in frame at time t, f_x is the partial derivative of f in the x direction evaluated at pixel (x, y) in frame at time t, and f_y is the partial derivative of f in the y direction evaluated at pixel (x, y) in frame at time t, and f_t is the partial derivative of f in the x direction evaluated at pixel (x, y) in frame at time t. Using finite differences, for each pixel save one row/column, f_x and f_y can be approximated. According to our objective, for the correctly chosen dx, dy:
$$df = f(x + dx, y + dy, t + dt) - f(x, y, t)$$

Therefore,
$$f_x dx + f_y dy - df = -f_t dt$$
This equation can be written for every pixel in the frame, save one row and one column. Using linear least squares, the best-fit dx, dy, df can be found. Each frame from frame 1 to frame $n_t - 1$, where n_t is the total number of frames, will have different values of dx, dy, df.

The optical flow algorithm is applied to image frames that have been first morphologically opened with a disk structuring element of 5 pixels (to remove small artifactual objects) and Gaussian filtered (to blur/smooth the image) with a width of 10 pixels. Applying the optical flow protocol always resulted in an adequately stabilized image, which implies that our assumptions were adequately satisfied.

Next, the stabilized image was segmented to detect the nuclei. If the image sequence was taken with both Dl-GFP and H2A-RFP (to mark the nuclei), then the RFP channel was used to segment the nuclei. If only Dl-GFP was imaged, then the GFP channel was used, which only works if the focus is on the ventral side. To detect the nuclei, the entire image sequence was summed to find an aggregate frame (Figure S3D). This aggregate frame was morphologically eroded by the pixel equivalent of 2 microns, then morphologically dilated by the pixel equivalent of 0.5 microns. This resulted in an aggregate frame where small, non-nuclear objects were removed, but objects representing nuclei that remain were ensured to have a diameter of at least 0.5 microns. After Gaussian blurring with a width of the pixel equivalent of 0.5 microns (Figure S3E), a watershed algorithm was applied to the complement of the blurred image. The watershed image was a label image, where the pixels corresponding to each nucleus plus the cytoplasm surrounding it were given a distinct numerical label (Figure S3F). The boundaries between cytoplasmic compartments were pixels of zero intensity (white in Figure S3F,G). This watershed matrix served to delineate the boundaries between cytoplasmic compartments for the remainder of the analysis.

We then analyzed each individual frame of the image sequence. We split the frame into the pixel sets that corresponded to each cytoplasmic compartment found by watershed. Each cytoplasmic compartment was hard-thresholded at 35% intensity. The remaining object with the largest area was declared to be the nucleus, after eroding by a disk of three pixels (Figure S3G, blue). All pixels outside of the largest-area object (pre-erosion) were also eroded by a disk of three pixels then declared to be cytoplasm (Figure S3G, orange). The two erosion operations were performed to get conservative estimates of what is the nucleus and what is the cytoplasm. This process was repeated for each cytoplasmic compartment in each frame of the image sequence, which resulted in our ability to track the nuclear and cytoplasmic fluorescence in the Dl-GFP channel, over time (Figure S3H).

The timecourse data for the nuclear intensity were then fit to the solution of a differential equation that described the nuclear concentration of Dl:

$$\frac{d[Dl]_{nuc}}{dt} = k_{in}[Dl]_{cyt} - k_{out}[Dl]_{nuc}$$

…where $[Dl]_{nuc}$ and $[Dl]_{cyt}$ are the nuclear and cytoplasmic concentrations of Dl, respectively, and k_{in}, k_{out} are the nuclear import and export rate constants for Dl, respectively. The cytoplasmic concentration timecourse measurements served as input to this equation, and the nuclear concentration timecourse measurements were the target of the fit.

For a general function $[Dl]_{cyt}(t)$, the solution to this differential equation is:

$$[Dl]_{nuc}(t) = c_0 \exp(-k_{out}t) + k_{in}\exp(-k_{out}t) \int_0^t [Dl]_{cyt}(t') \exp(k_{out}t') \, dt'$$

…where $t = 0$ corresponds to the time point directly after bleaching, and c_0 is an adjustable parameter that corresponds to the concentration of nuclear Dl at time $t = 0$. The fits were performed with Matlab's lsqcurvefit function.

Parameter Estimation

Some biophysical parameters that appear in our model have crude estimates available. These estimates helped us set acceptable bounds for variation of these parameters in our parameter search scheme. First, photobleaching experiments (this work and Delotto et al., 2007) help to constrain k_{in} and k_{out} (from the full model; these correspond to dimensionless parameters ζ and ξ). Our photobleaching observations put our estimate of both $k'_{in} = k_{in} A_n/V_n$ and $k'_{out} = k_{out} A_n/V_n$ at roughly 0.1-0.4 min^{-1} (Fig S3I). Analysis of photobleaching recovery curves found in Delotto et al., 2007 give an estimate of k'_{out} as 1 min^{-1}. Note that k_{in} and k_{out} in the simplified model are the same as k'_{in} and k'_{out} discussed here.

The dimensionless parameters ζ and ξ are defined as:
$\zeta = (A_n^{14}T/V_n^{14})k_{in} = k'_{in}T$ and $\xi = (A_n^{14}T/V_n^{14})k_{out} = k'_{out}T$, where in both cases, the final equality holds true during nuclear cycle 14, and where $T = 1$ min. of these Therefore, preliminary estimates of these parameters are $\zeta \sim 0.1 - 0.4$ and $\xi \sim 0.1 - 1$.

However, recall that there is a ζ for Dl and a ζ for Dl/Cact complex (and similar for ξ). Because of this, we did not have utter confidence in using the photobleaching estimates to directly constrain the $\zeta's$ and $\xi's$. Instead, we assume the estimation of k'_{in} and k'_{out} from these experiments is some weighted average between those parameters for free Dl and Dl/Cact complex with unknown weightings. Therefore, we took these estimates as justification to center our evolutionary search algorithm (for the full model) around 10^0. For the simplified model, we held $K_{eq} \equiv k_{in}/k_{out}$ fixed at 4, which roughly reflects the ratio of nuclear to cytoplasmic Dl near the ventral midline.

Next, there are several rough estimates and/or scaling arguments available for the intercompartmental exchange coefficients, λ. As defined above, $\lambda = k_m A_n^{14} T/V_n^{14}$, where k_m is the mass transfer coefficient (in dimensions of length per time), A_n^{14} and V_n^{14} are the surface area and volume of a nuclear cycle 14 nucleus, respectively, and $T = 1$ min. If the nucleus is roughly spherical and its radius is roughly 5 microns, then this definition implies $k_m = \lambda \times 1$ micron/min $\sim \lambda \times 10^{-6}$ cm/s. Engineering literature suggests that mass transfer coefficients of proteins through membranes, in protein separations processes, can span $10^{-3} - 10^{-6}$ cm/s, which implies λ could fall within the range of order 1 up through 10^3. On the other hand, theoretical scaling arguments in which λ is controlling the shape of a gradient suggest λ could fall within the range of 10^{-4} through order 1. As we have no reason to believe that the literature measurements (in separations) represent a lower bound, nor do we need to assume that a simple scaling argument represents the upper bound (considering the complexity of our model), it is not unreasonable to allow in our parameter searches several decades of variation centered on 10^0 (see Fig 2B).

As further confirmation of this, we used our photoactivation experiments to give a very crude estimate of the effective diffusivity. We observed that Dl moves over 7-10 nuclear diameters in the time span of 90 minutes. As the average distance between the centroids of two neighboring nuclei is roughly 7 μm, this translates to an effective diffusivity of ~0.4-0.9 μm^2/s and a time scale to cross one cell diameter that is on the order of minutes. However, this crude estimate stems from an experiment not designed specifically to measure the diffusivity, and also does not take into account the changing distances between nucleocytoplasmic compartments due to mitosis during the 90 min period. Even so, this estimate also suggests that the λ values be centered around 10^0. Using scaling arguments, we suggest the effective diffusivity is on the order of 1 micron^2 per second. As detailed above, the relationship between effective diffusivity and "lambda" is as follows:

$$D_{eff} = \lambda \frac{A_c V_n^{14}}{V_c A_n^{14}} \frac{(\Delta x)^2}{T}$$

…where A_c is the surface area between nucleocytoplasmic compartments available for intercompartmental exchange, V_c is the volume of cytoplasm inside a nucleocytoplasmic compartment (so, total volume minus the volume of the nucleus), Δx is the diameter of a nucleocytoplasmic compartment (roughly 7 microns), and, as before, A_n^{14} and V_n^{14} are the surface area and volume of a nucleus, and $T = 1$ min. This relationship can be rearranged to give

$$D_{eff} \frac{T}{(\Delta x)^2} = \lambda \frac{A_c V_n^{14}}{V_c A_n^{14}}$$

…where the left hand side is approximately equal to one (dimensionless). Assuming each nucleocytoplasmic compartment is roughly cylindrical with a radius R and height h, the right hand side becomes:

$$\frac{\lambda}{0.75\,\Delta x/r - 24/(h\Delta x)} \sim 1$$

If $\Delta x = 7$ microns, $r = 2.5$ microns, and $h = 15$ microns, then this means lambda ~ 2. However, recall that this was originally based on a very rough estimate for D_{eff} from an experiment that was not designed to estimate this parameter. However, this can be taken as an independent argument that the range of possible values for λ should be centered around 10^0.

Fitting Dl gradients and sna peaks
Each Dl nuclear gradient curve was fit to a modified Gaussian-like curve with five adjustable parameters:
$$Dl(x) = A\exp(-(x-\mu)^2/(2\sigma^2)) + B - M|x|$$
Here A is the gradient amplitude, B represents the basal levels, σ is the gradient width, and M is the (typically non-zero) slope of the tails of the gradient. The parameter μ is the location of the ventral midline within the image. See also (Liberman et al., 2009; Reeves et al., 2012; Trisnadi et al., 2013) for more information.

Plots of normalized Dl gradients were generated by subtracting B value and 70% of the M value, then dividing by A. In other words:

$$Dl_{normalized}(x) = \frac{Dl(x) - (B - 0.7M)}{A}$$

Only 70% of the slope was subtracted because it is the average between the value of the gradient tail at $x = 1$ (lowest value) and at $x = 0.4$ (where the contribution from the Gaussian terms in wildtype embryos become negligible).

The average normalized intensity curve was generated by averaging the normalized curves of all embryos in the specified genotype. After this procedure, the averaged curve was not re-normalized, which is why these averaged curves do not always fall exactly between zero and one.

The width of the *sna* domain for each embryo was computed as described in (Liberman et al., 2009; Reeves et al., 2012; Trisnadi et al., 2013). Briefly, a canonical profile of *sna*, called $sna_0(x)$, was generated by averaging the *sna* domain of many wildtype embryos together. Next, local background subtraction was performed (top hat morphological transform) with a structuring element of width of 25% DV axis length, which removes background intensity variations that are wider than the structuring element. Peaks of *sna* expression are preserved in height and width because they are narrower than the structuring element. Finally, all *sna* expression domains were then fit to this canonical profile by the following equation:

$$sna(x) \approx A\, sna_0(x/\delta) + B,$$

where A and B are the amplitude and background levels, and δ is a "stretching factor" that defines how wide or narrow the individual *sna* expression domain is with respect to the canonical form. If $\delta > 1$, then the individual profile is wider than the canonical form, and if $\delta < 1$, then it is narrower. The final width measurement of the *sna* domain was computed as the width of the canonical profile (measured at half-max) times δ. In a similar manner to Dl, when average *sna* curves are generated, the resulting curves were not re-normalized, which again is why these averaged curves do not always fall exactly between zero and one.
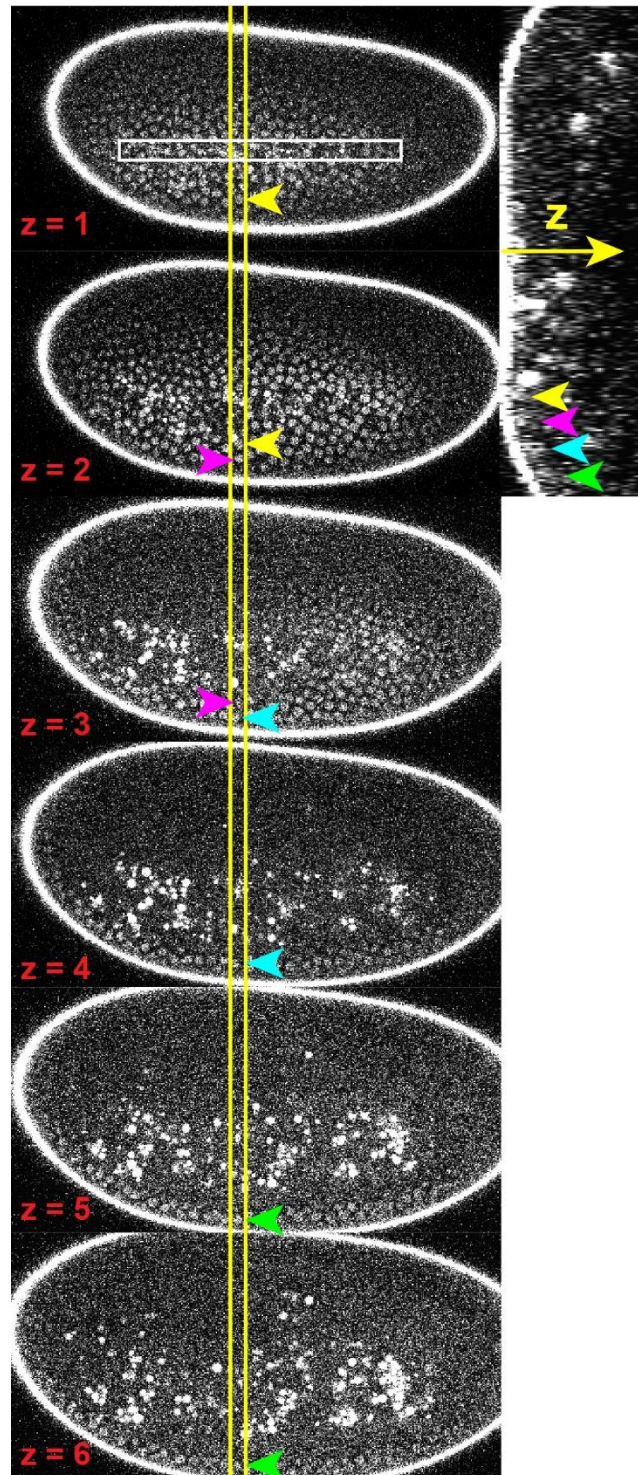
Figure S1: Photo-Activated Dl Can Be Seen at Least Seven Nuclei away from the Activation Box on the Ventral Side, Related to Figure 1. Six z-slices (xy sections) of embryo found in Figure 1H are depicted, as well as a yz-section (right), where the arrow indicates the z-direction. Yellow bars indicate the x-coordinate fixed in the yz-slice. Arrowheads point to individual nuclei. Arrowheads of the same color refer to the same nucleus in different views. Three nuclei can be counted between the activation box and the nucleus referenced by the yellow arrowhead.
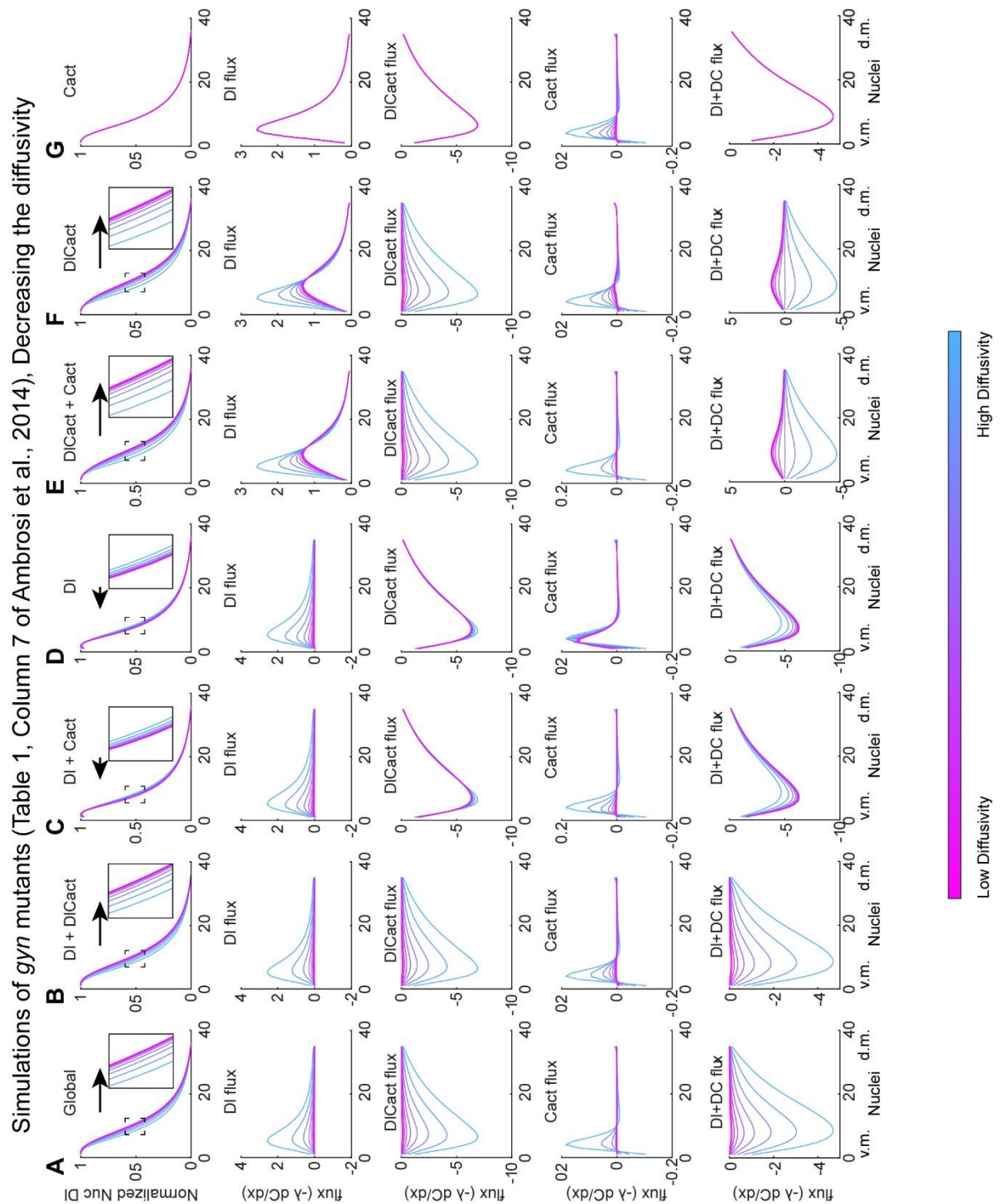
Figure S2: Previous Models of the Dl Gradient Also Exhibit Shuttling, Related to Figure 2. (A) The model from Ambrosi et al., 2014 predicts the widening of the gradient when the diffusivity of all three species (Dl, Cact, and Dl/Cact complex) is simultaneously lowered (top panel; see arrow for direction and inset for better view of the changes to the gradient). Note that in the Ambrosi model, there is only one diffusivity parameter, which dictates the mobility of all three species. This

widening is apparently the result of changes to the Dl/Cact complex flux, as the flux of Dl is towards the dorsal midline (curves are above zero in the second panel), yet the flux of Dl/Cact complex is towards the ventral midline (curves are below zero in the third panel). The flux of Cact has minimal effect (based on order of magnitude; fourth panel). (B) If the diffusivities of both Dl and Dl/Cact complex are lowered, the widening effect is also present. The fluxes are qualitatively similar to (A). (C) If the diffusivities of Dl and Cact are both lowered, the gradient becomes slightly narrower. This highlights the fact that the widening (shuttling) effect comes from Dl/Cact complex. Indeed, in this case, the Dl/Cact complex flux is only minimally effected by this change (third panel), so the narrowing effect must come from the change in the Dl flux (second panel). (D) Changing the diffusivity of Dl only has nearly the same effect as that seen in (D). (E) Changing the diffusivities of Dl/Cact complex and Cact widens the gradient, to a greater extent compared to those seen in (A) and (B). This effect again must be the product of the change to the flux in Dl/Cact complex (third panel), as the change to the Dl flux is minimal (second panel). (F) If the diffusivity of only Dl/Cact complex is changed, the result is nearly identical to that seen in (E). (G) Changing the diffusivity of Cact alone has an insignificant effect on the Dl gradient. Parameter set used can be found in Table 1, Column 7 of Ambrosi, et al., 2014, which corresponds to the simulation for the *gyn* mutant. Colorbar at bottom highlights that lower diffusivities are indicated by magenta. (Note that the first/last simulated nucleus in not exactly at DV = 0/1, respectively, because of the discretization mesh. Thus, graphs of the flux do not necessarily start and end at exactly zero for the DV coordinate.)
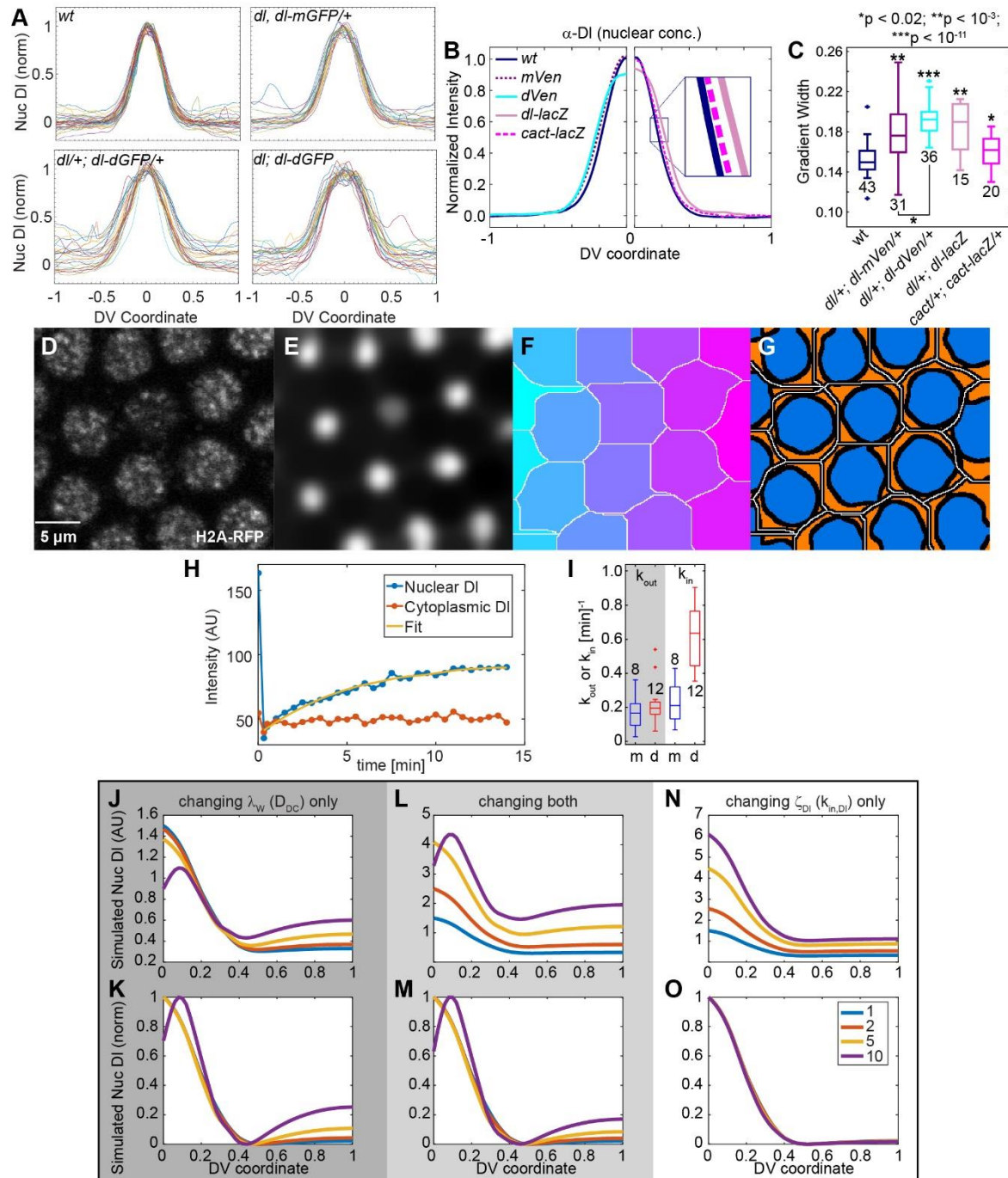
Figure S3: Decreasing Diffusion of Dl/Cact Widens the Dl Gradient, Related to Figure 3. (A) Full data sets of Dl gradients that were averaged to result in the curves found in Fig. 3A. (B) Normalized average Dl nuclear gradients in embryos from several different genetic backgrounds. Plots are only shown for half of the DV axis so that more gradients can be plotted without too many being plotting on top of each other. Genetic backgrounds include wildtype (both sides of graph), *dl/+; dl-mVen/+* (mVen; left), *dl/+; dl-dVen/+* (dVen; left), *dl/+; dl-lacZ* (dl-lacZ; right), and *cact/+; cact-lacZ/+* (cact-lacZ; right) embryos. Inset shows more clearly that *dl-lacZ* and *cact-lacZ* are slightly

wider than wt. Legend: full genotypes depicted at bottom of boxplot in (C); color scheme the same between (B) and (C). (C) Gradient widths in the embryos from (B). Note that the same "allelic series" approach is also valid for Dl-Venus constructs. Embryos from *dl/+; dl-mVenus/+* mothers have slightly wider gradients than wildtype, (σ = 0.179 ± 0.005; mean ± s.e.m.), while embryos from *dl/+; dl-dVenus/+* mothers had further widened Dl gradients (σ = 0.192 ± 0.003). Furthermore, both *dl-lacZ* and *cact-lacZ* expand the gradient. In particular, the fact that *cact-lacZ* expands the Dl gradient indicates that that this fusion affects the accumulation of Dl. (D) Example aggregate frame (sum of all frames in the nuclear channel) for bleaching experiment (*dl/+; dl-mGFP/+* embryo shown). (E) Aggregate frame after erosion, dilation, and Gaussian blurring. The complement of this image was used for a watershed operation. (F) Output of watershed protocol. Each cytoplasmic compartment is individually labeled with a different numerical value (shown here as a different color). White pixels delineate boundaries between the compartments. (G) Segmented image of frame 1. Each compartment is analyzed individually and is subdivided into nucleus (blue) and cytoplasm (orange). The black pixels belong to neither, due to labeling nucleus and cytoplasm conservatively. (H) Timecourse of nuclear (blue) and cytoplasmic (red) Dl for one photobleaching experiment. The least-squares fit is shown in yellow. (I) Boxplot of measured values of k_{out} (left side, gray) and k_{in} (right side, white) for *dl/+; dl-mGFP/+* embryos (m; blue) or *dl/+; dl-dGFP/+* embryos (d; red). Values in inverse minutes. The difference in k_{out} between mGFP and dGFP is not significant, whereas the difference in k_{in} clearly is: k_{in} for dGFP is roughly twice as large as that for mGFP. (H-O) Model analysis of perturbing the import rate, the diffusion rate, or both. This analysis was performed to determine whether the difference in import rate could explain the difference in gradient width. (J) Effect of lowering the diffusivity of Dl/Cact complex on the nuclear Dl gradient (simulation using the "Full model"). The hallmark shuttling phenotype is observed. (K) Curves from (J), but normalized. (L) Same as (J), but k_{in} is increased by the same fold-change as the D_{DC} is decreased. The hallmark shuttling phenotype is still observed. (M) Curves from (L), but normalized. (N) Same as (L), but only k_{in} is perturbed (D_{DC} is held fixed). The shuttling phenotype is not observed. Thus, a shuttling phenotype is observed when diffusion is altered, but not when only capture is altered. (O) Curves from (N), but normalized.
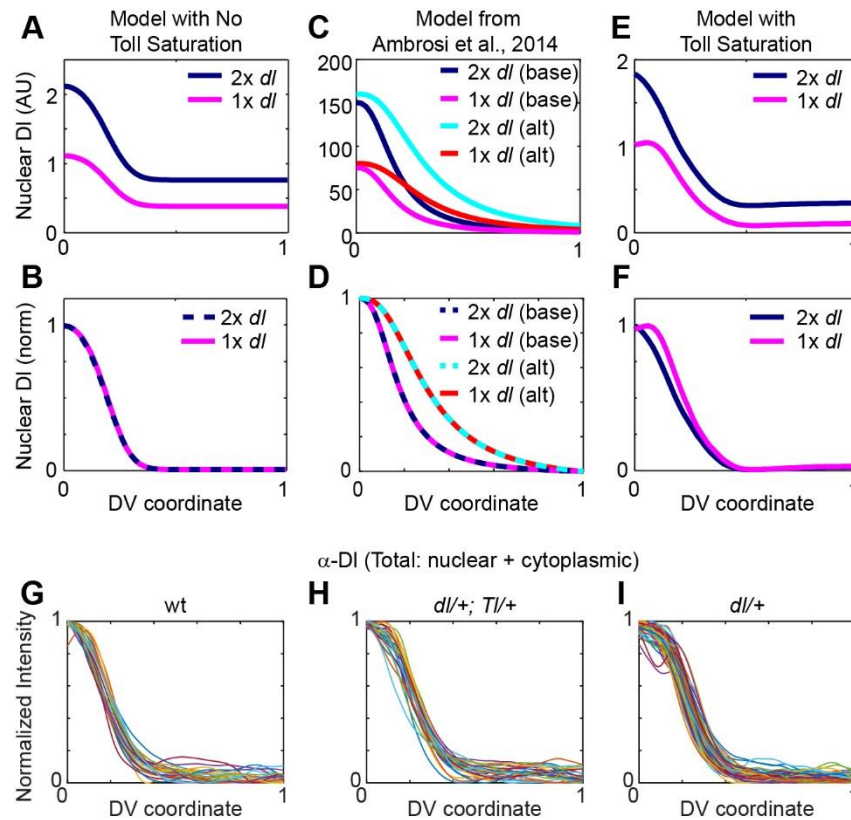
Figure S4: Updated Model Formulation Recreates the *dl* Heterozygous Phenotype, Related to Figure 4. (A) Plots of simulated Dl gradients for wildtype (2x *dl*) and *dl/+* (1x *dl*) embryos in a model with no toll saturation taken into account (O'Connell and Reeves, 2015). (B) Same plots from (A), but normalized. The two plots collapse onto each other. (C) Same as (A), but for a different model formulation found in (Ambrosi et al., 2014). Two separate parameter sets are represented: base and alternative. See Supplemental Experimental Methods for explanation. (D) Same plots from (C), but normalized. As with (A,B), the plots from corresponding parameter sets collapse onto each other. (E) Same as (A), but for a model that considers the possibility of active Toll saturation ("Full model" formulated here). Even without normalization, the difference in peak shape can be seen. (F) Same plots from (E), but normalized. The difference in peak shape is more clearly seen. Similar results can be obtained using the simplified model with Toll saturation. (G-I) Full data sets of Dl gradients that were averaged to result in the curves found in Fig. 4H.
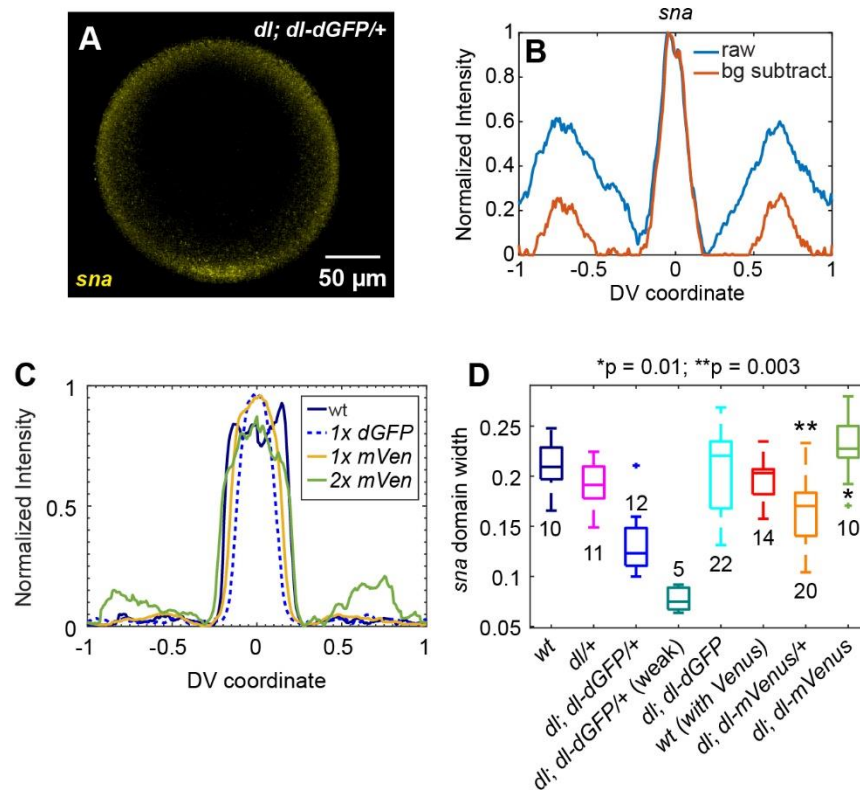
Figure S5: Severe Defects in Dl Gradient Formation from Simultaneous Shuttling Perturbations Result in Compromised *sna* Domains, Related to Fig. 5. (A) Representative embryo from among the five *dl; dl-dGFP/+* embryos that expressed sna very weakly. The *sna* domains in these embryos could not be detected by unsupervised image analysis (Trisnadi et al., 2013). Manual analysis was required to extract the width of the *sna* domain. (B) Quantification of the sna domain from embryo in (A). The width of the *sna* domain in this embryo was measured as the half-width of the peak at half-max. The red curve is background subtracted with a structuring element of the size of 25% of the DV axis arclength. This procedure preserves the peak (which is narrower than 25% DV axis arclength) while removing most of the noise outside of the peak. (C) The average *sna* domain from wildtype, *dl; dl-dGFP/+* (1x *dl-dGFP*), *dl; dl-mVen/+* (1x *dl-mVen*), and *dl; dl-mVen* (2x *dl-mVen*) embryos. Of these, only *dl; dl-dGFP* are non-viable, and these also have a visibly narrower *sna* domain. Wildtype and *dl; dl-dGFP* curves the same as found in Fig. 5C, and do not include the "weak" sna domain embryos found in (A,B). (D) Boxplot of *sna* domain widths for embryos of various genotypes depicted at bottom. The first, second, third, and fifth box-and-whisker sets are also found in Fig. 5E. This boxplot is for further comparison of the "weak" *sna* domains (embryos in A,B) and embryos with *dl-mVenus* constructs. Most relevant pair-wise statistical tests can be found in Fig. 5E. The "wt (with Venus)" corresponds to measurements of wildtype embryos that were stained with the mVenus embryos in the same experiment. These are statistically indistinguishable from the wildtype population in the first column. Asterisks indicate pair-wise statistical difference from "wt (with Venus)" population.
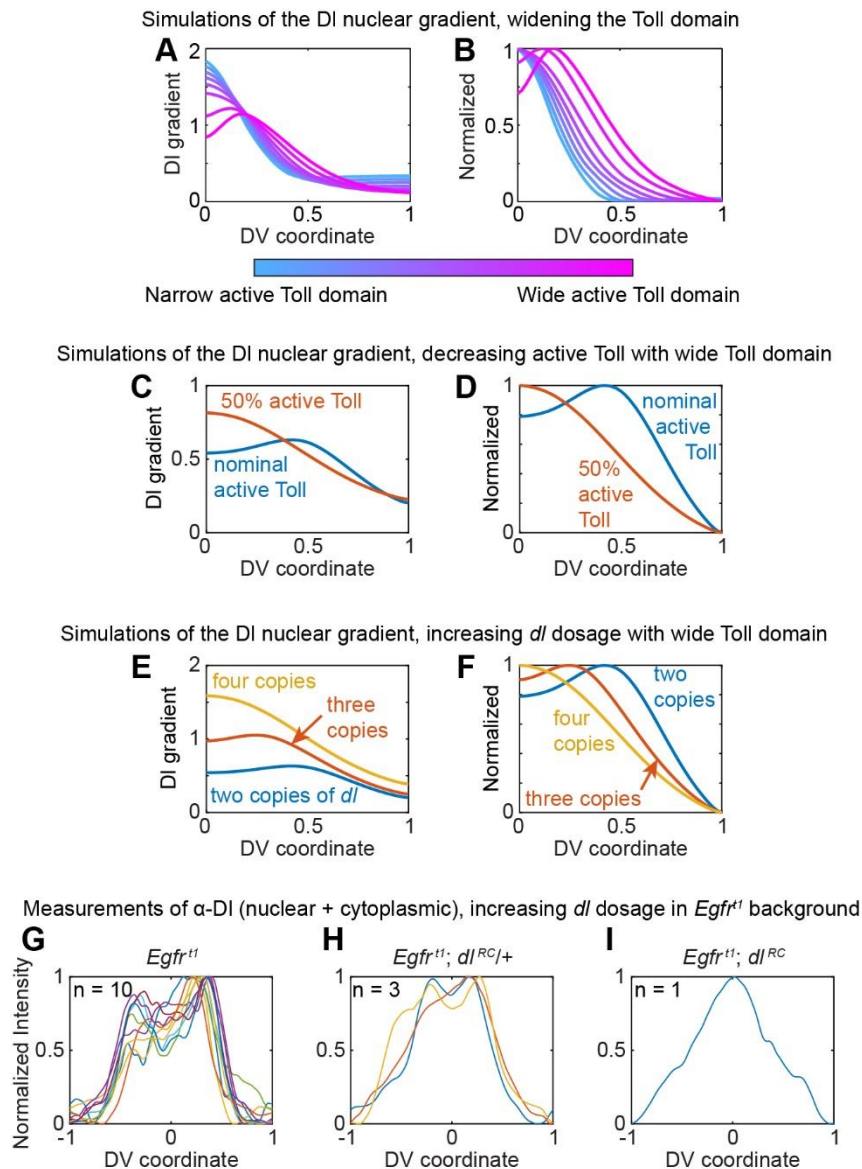
Figure S6: Rescuing The Single Dl Gradient Peak in Embryos with Wide Toll Domains, Related to Fig. 6. (A,B) Simulations of the Dl nuclear gradient, using the "Full model", with different widths of the Toll domain. Note that wider Toll domains result in wider gradients, and split peaks when the Toll domain is wide enough. The non-normalized plots are in (A), and normalized in (B). Colorbar indicates spectrum of Toll domain width. Note this colormap runs opposite to those for the diffusivity in Figs 2 and S2, as in all plots with this colormap, moving towards magenta refers to larger shuttling perturbations. Similar results can be obtained using the simplified model with Toll saturation. (C,D) Simulations of the Dl gradient with a wide Toll domain and decreased Toll receptors. The shuttling hypothesis with Toll saturation predicts that the split peak of the Dl gradient found when the Toll domain is widened is abolished if active Toll levels are reduced by 50%. This can be seen in both the non-normalized (C) and normalized (D) plots. (E,F) Simulations of the Dl gradient with a wide Toll domain and with three different *dl* dosages: wt (2x), 3x, and 4x. Increasing *dl* dosage results in a tall gradient (E), but also one with a less severe split peak (3x) or a

single peak (4x), as seen in the normalized plot (F). (G,H,I) Measurements of total dl (nuclear + cytoplasmic) in single *Egfr*[*t1*] embryos (maternal genotype) with two copies of *dl* (G), three (H), and four (I). The averaged gradients from these sets of embryos can be seen plotted in Fig. 6E. Note that one outlier for *Egfr*[*t1*] was not included in part (G).
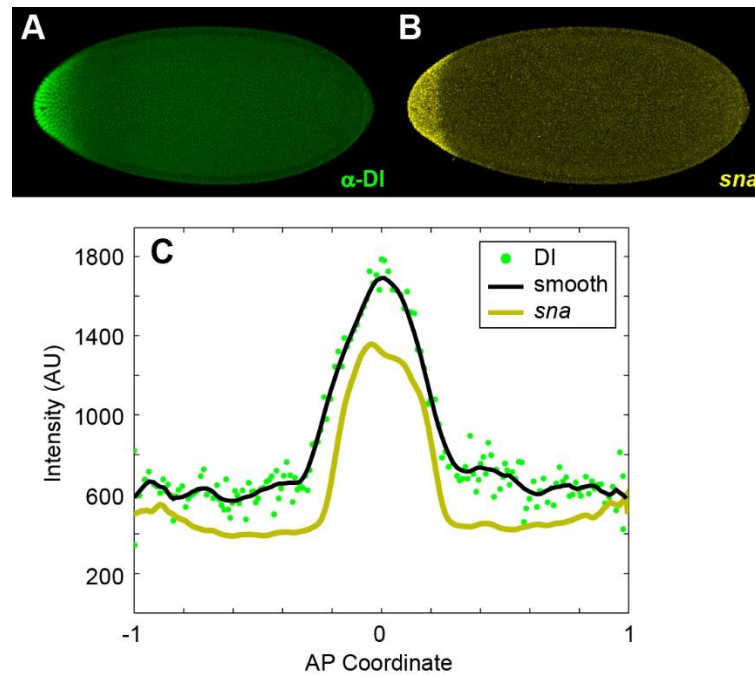

Figure S7: Embryos with AP Dl Gradients Under the Control of a Weaker (bcd) Promoter Do Not Exhibit the Double-Peak Phenomenon, Related to Figure 7. For this experiment, five embryos were analyzed, four of which had a detectable peak at the anterior pole. Note that the x-axis in (C) is the anteroposterior axis, not the dorsal-ventral axis as has been commonly used in the rest of this document.

Supplemental Tables

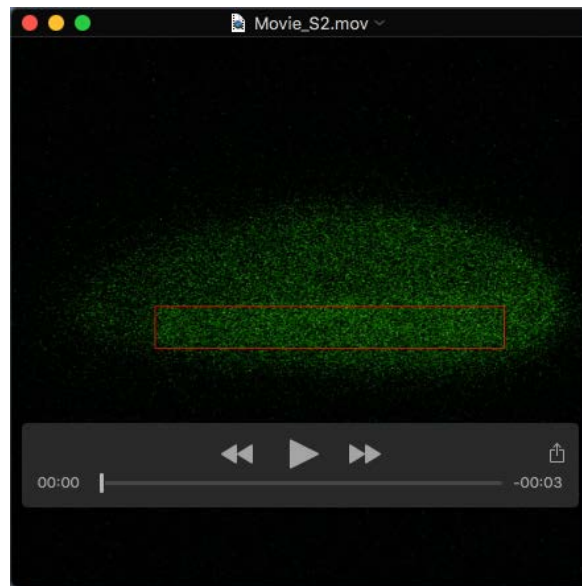**Table S1.** List of Primers Used for BAC Recombineering and Sequencing.

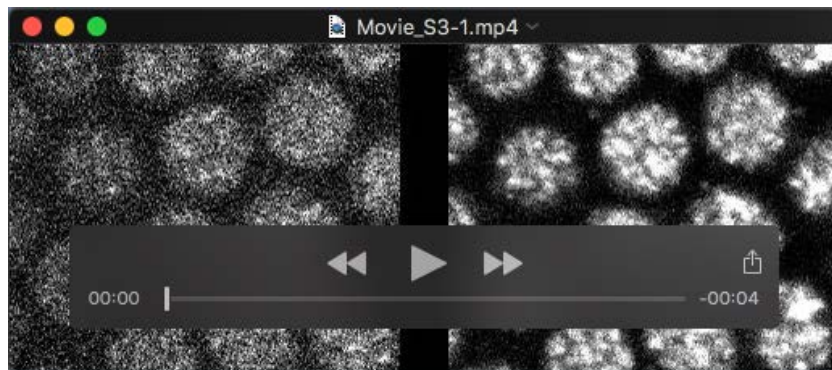Click here to Download Table S1

Supplemental Movies
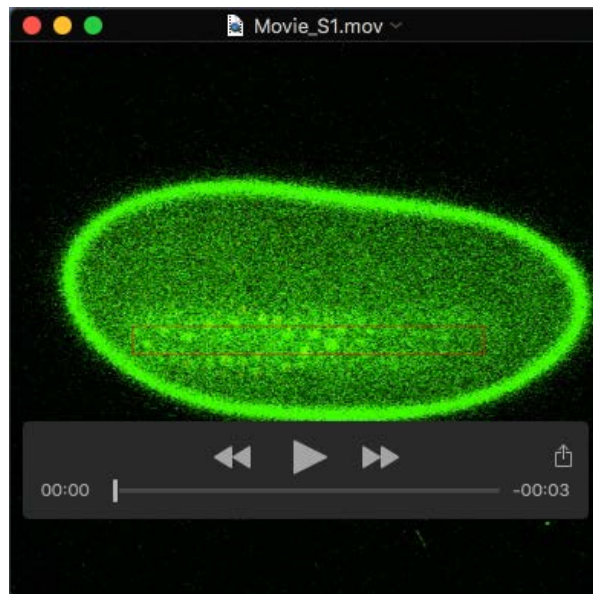
Movie S1: A Z-stack of an Embryo with Dl-paGFP That Has Been Activated Near the Ventral Midline, Related to Figure 1.

Movie S2: A Z-stack of an Embryo with Dl-paGFP That Has Been Activated on the Dorsal Side, Related to Figure 1.

Movie S3: Time course of a photobleaching experiment with a *dl/+;dl-mGFP/+* embryo. Left side: Dl-mGFP fluorescence. Right side: H2A-RFP fluorescence. Frames are 30 s apart. Movie played at 7 frames per second. Related to Figure 3.